

ANL/APS/TB-54

**DOSE CALCULATIONS USING MARS FOR
BREMSSTRAHLUNG BEAM STOPS AND COLLIMATORS IN APS
BEAMLINE STATIONS**

Jeffrey C. Dooling
Accelerator Systems Division
Advanced Photon Source

August 2010

This work is sponsored by the US Department of Energy
Office of Science

The submitted manuscript has been created by UChicago Argonne, LLC, Operator of Argonne National Laboratory ("Argonne"). Argonne, a U.S. Department of Energy Office of Science laboratory, is operated under Contract No. DE-AC02-06CH11357. The U.S. Government retains for itself, and others acting on its behalf, a paid-up nonexclusive, irrevocable worldwide license in said article to reproduce, prepare derivative works, distribute copies to the public, and perform publicly and display publicly, by or on behalf of the Government.

Acknowledgements

I wish to express my gratitude to Harold J. Moe, for many helpful and insightful discussions on radiation physics. I am indebted to Patricia Fernandez, Chair of the Advanced Photon Source Radiation Shielding Safety Committee, for her assistance in guiding this work. Thank you to Louis Emery for his thorough reading of the initial draft and his important suggestions. Thanks to all members of the RSSC for their useful comments.

I am grateful to the members of the External Review Committee for playing a vital role assessing the document and providing comments, especially Paul Berkvens of the ESRF who chaired the committee. In addition to Paul, the committee included Johannes Bauer (SLAC), Michael Borland (APS), Nikolai Mokhov (FNAL) and Giuliana Tromba (Elettra, Trieste) and I thank each of them. Finally, Efim Gluskin should be acknowledged as the driving force behind the creation and completion of this document.

Jeffrey C. Dooling
August 1, 2010

Executive Summary

The Monte Carlo radiation transport code MARS is used to model the generation of gas bremsstrahlung (GB) radiation from 7-GeV electrons which scatter from residual gas atoms in undulator straight sections within the Advanced Photon Source (APS) storage ring. Additionally, MARS is employed to model the interactions of the GB radiation with components along the x-ray beamlines and then determine the expected radiation dose-rates that result. In this manner, MARS can be used to assess the adequacy of existing shielding or the specifications for new shielding when required.

The GB radiation generated in the “thin-target” of an ID straight section will consist only of photons in a $1/E$ -distribution up to the full energy of the stored electron beam. Using this analytical model, the predicted GB power for a typical APS 15.38-m insertion device (ID) straight section is 4.59×10^{-7} W/nTorr/mA, assuming a background gas composed of air ($Z_{\text{eff}}=7.31$) at room temperature (293K). The total GB power provides a useful benchmark for comparisons between analytical and numerical approaches. We find good agreement between MARS and analytical estimates for total GB power. The extended straight section “target” creates a radial profile of GB, which is highly peaked centered on the electron beam. The GB distribution reflects the size of the electron beam that creates the radiation. Optimizing the performance of MARS in terms of CPU time per incident trajectory requires the use of a relatively short, high-density gas target (air); in this report, the target density is $\rho L = 2.89 \times 10^{-2}$ g/cm² over a length of 24 cm.

MARS results are compared with the contact dose levels reported in TB-20, which used EGS4 for radiation transport simulations. Maximum dose-rates in 1 cc of tissue phantom form the initial basis for comparison. MARS and EGS4 results are approximately the same for maximum 1-cc dose-rates and attenuation in the photon-dominated regions; for thicker targets, however, the dose-rate no longer depends only on photon attenuation, as photoneutrons (PNs) begin to dominate.

The GB radiation-induced photoneutron measurements from four different metals (Fe, Cu, W, and Pb) are compared with MARS predictions. The simulated dose-rates for beamline 6-ID are approximately 3-5 times larger than the measured values, whereas those for beamline 11-ID are much closer. Given the uncertainty in local values of pressure and Z , the degree of agreement between MARS and the PN measurements is good.

MARS simulations of GB-induced radiation in and around the FOE show the importance of using actual pressure and gas composition (Z_{eff}) to obtain accurate PN dose. For a beam current of 300 mA, extrapolating pressure data measured in previously published studies predicts an average background gas pressure of 27 nTorr. An average atomic number of $Z_{\text{eff}}=4.0$ is obtained from the same studies. In addition, models of copper masks presently in use at the APS are included. Simulations show that inclusion of exit masks make significant differences in both the radiation spatial distribution within the FOE, as well as the peak intensity.

Two studies have been conducted with MARS to assess shielding requirements. First, dose levels in contact with the outside wall of the FOE are examined when GB radiation strikes Pb or W beam stops of varying transverse size within the FOE. Four separate phantom regions are utilized to measure the dose, two at beam elevation and two at the horizontal beam position. The first two phantoms are used for scoring FOE dose

along the outside and back walls, horizontally; the second two collect dose on the roof and vertically on the back wall. In all cases, the beam stop depth is maintained at 30 cm. Inclusion of front end (FE) exit masks typically cause a 1-2 order-of-magnitude increase in the dose-rates relative to the case with no masks. Masks place secondary bremsstrahlung sources inside the FOE, and therefore they must be shielded appropriately. The MARS model does not fully account for all shielding present in the hutches; localized shielding is employed in individual hutches. Typically, a collimator, placed downstream of the FE exit masks, mitigates the possible increase in dose. Regarding beam stop transverse size, a modest reduction in dose on the back wall is noted as the stop dimension (square cross section) is increased from 12 cm to 24 cm.

In the second study, the thickness of Pb required to shield against the GB extremal ray is determined. In this study, we are interested in finding the thickness of material necessary to add at the edge of a stop to adequately block GB radiation; therefore, we look at the case of no masks in order to have a well-defined GB beam edge. Simulations show the separation between the extremal ray and the edge of the shielding should be $2R_m$, where R_m is the Moliere radius. In the context of TB-20, therefore, an extremal ray should come no closer than 2.2 cm to the lateral edge in Pb. For W, the same argument sets the extremal ray shield edge separation at 1.3 cm.

Benchmarking studies were conducted comparing MARS with other relevant simulations. We first used MARS and EGS4 to examine the angular spread of the distribution with respect to target density. MARS distributions are seen to agree well with EGS. With MARS, a penalty is paid in terms of CPU time per initial trajectory with increasing target length for a constant target density. In terms of GB spectra, MARS is in good agreement with EGS4 above 10 MeV; however, an enhancement occurs at low energy (below 10 MeV) not present with EGS4. One cannot select a single interaction in MARS as can be done in EGS4 to limit low-energy interactions. Limiting these interactions is important since they normally do not occur in low-density targets, such as the residual gas of an ID straight section. MARS output tends to be somewhat noisy because of the inclusive approach taken to particle interactions. For example, in a binary reaction, only one path is followed, with twice the weight. Therefore in the generation of tertiary particles, such as PNs after a long chain of interactions, large fluctuations in weighting can occur. A comparison of PN production with FLUKA shows similarity in form with angle and energy, but the intensity predicted by MARS is lower. The author of the FLUKA study indicates a factor of 4π may be unaccounted for in one of the data sets. In addition, PN levels predicted by MARS are close to measured values. We hope to obtain an answer to the amplitude discrepancy question by running the FLUKA simulation locally. Photoneutron calibration aside, MARS output is in good agreement with other Monte Carlo programs.

Table of Contents

1. Introduction.....	1
2. Gas Bremsstrahlung Analysis.....	2
2.1 Gas Bremsstrahlung Power.....	3
2.2 Pair production.....	7
2.3 Gas Bremsstrahlung Dose Estimate.....	8
2.4 Gas Bremsstrahlung Beam Distribution.....	13
3. Contact Dose-rate—Comparison with TB-20.....	18
3.1 Description.....	18
3.2 x-y Histograms.....	20
3.3 y-z Histograms and Abel Inversion.....	22
3.4 Analysis.....	24
4. Photoneutron (PN) Production.....	26
4.1 Description.....	26
4.2 Previous PN Dose Measurements and Comparisons with MARS.....	28
4.3 Comments on PN Dose Measurements and Simulations.....	29
5. First Optics Enclosure (FOE) Studies.....	30
5.1 MARS Dose Determination.....	32
5.2 Effects of Masks in the FOE.....	34
5.3 FOE Beam Stop Transverse Dimensions and Material.....	36
5.4 Extremal Ray.....	38
6. Discussion and Summary.....	40
6.1 Dose Results.....	40
6.2 Computational Considerations.....	41
Reference.....	42
Appendix A: Benchmarking MARS.....	A-1
A-1. Comparisons of Gas Bremsstrahlung Photon Density with Target Density.....	A-1
A-2. GB Photon Density and Threshold Electron Energy.....	A-1
A-3 PN Production.....	A-3
A-4 Proton Beam Comparisons.....	A-5
References.....	A-8
Appendix B: TB-20 Extremal Ray Methodology—Results with MARS.....	B-1
Appendix C: Examples of MARS Input Files Used to Model the First Optics Enclosure..	C-1
MARS.INP.....	C-1
GEOM.INP.....	C-2
XYZHIS.INP.....	C-4

Dose Calculations using MARS for Bremsstrahlung Beam stops and Collimators in APS Beamline Stations

Jeffrey C. Dooling

Accelerator Systems Division, Advanced Photon Source

1. Introduction

A number of studies have been undertaken to quantify and measure the radiation produced at the APS and to specify the means necessary to mitigate its hazards. Specifically, APS Technical Bulletins (TB), TB-7 [1], TB-20 [2], TB-21 [3], and TB-44 [4] provide physical and engineering guidance regarding radiation source strength, material properties, and shielding requirements. These calculations used empirical formulas and the tracking program EGS4, which treats photons and electrons, but not neutrons. Neutron fluences, measured in two undulator insertion device (ID) beamlines [5,6], 6-ID and 11-ID, are compared here with MARS simulations. The availability of MARS gives us an opportunity to make calculations with all particles together, as well as to evaluate more complete geometries; taken together, we expect MARS to provide us with a more accurate prediction of the radiation environment in the beamlines due to the production of high-energy bremsstrahlung.

MARS [7,8] is a group of freely available but closed source Monte Carlo programs used for the description of high-energy particle transport through matter. It has been employed for detector modeling, production estimates (such as antiprotons), and radiation dose calculations. It describes the production and interaction of leptons, hadrons, photons, and heavy ions. In the present application, interest in MARS is focused on the interaction of 7 GeV electrons in the APS storage ring (SR) with various forms of matter that may be encountered and the radiation resulting from those interactions. For example, MARS is employed to model the generation of gas bremsstrahlung radiation as the electron beam scatters from residual gas in undulator straight sections, as well as the interactions of this radiation with components along the x-ray beamlines. Presently we are using MARS version 15, release 07 (last updated May 1, 2009).

The document is structured as follows: After a brief introduction in section one, the second section focuses on analysis of the gas bremsstrahlung (GB) source (i.e., spectral and spatial distribution of photons produced in the forward direction from stored beam interacting with residual gas). Analytical, numerical, and empirical bremsstrahlung source descriptions are compared. In section three, earlier EGS4 results presented in TB-20 are given alongside recent MARS simulations estimating the dose in a tissue phantom in contact with a heavy metal beam stop. Dose is obtained as the stop, composed of either Pb or W, is varied in thickness. MARS estimates of GB-induced photoneutron (PN) production are compared with earlier measurements in section four. Residual gas effective atomic number and pressure in the undulator straight sections, as well as beam alignment and collimation, are shown to play important roles in the prediction of GB-induced PN production. In section five, the first optics enclosure (FOE) geometry formerly presented in TB-7 is modeled in MARS. The required transverse size of the GB (“white”) beam stop is examined, as is the shielding separation necessary for the extremal ray specified in TB-20. We see that elevated pressure in the undulator beamline must be

considered due to its dependence on electron beam current. Discussion of MARS simulation results and comparisons with previous studies is summarized in section six.

The present document is meant to address dose-rate levels that may result from stored-beam fast electrons passing through the residual gas of an undulator vacuum vessel at the APS. Additional benchmarking comparisons of MARS with EGS4 and FLUKA simulations may be found in Appendix A. Examples of some of the MARS input files are given in Appendix C; these include the MARS.INP, GEOM.INP, and XYZHIS.INP files for the FOE discussed in Section 5.

Unless otherwise noted, the low-energy cutoffs or thresholds in MARS computations for photons, electrons, and positrons are all 0.2 MeV; the threshold for neutrons is 0.1 MeV; and for charged hadrons and muons, 1.0 MeV.

2. Gas Bremsstrahlung Analysis

In the first part of this section we will compare the power and dose-rate from gas bremsstrahlung (GB) photons calculated with an analytical formula, a MARS simulation, and a semi-empirical formula used in TB-20 and LS-260 [9]. Some discrepancies are revealed. A brief discussion of pair production is given. Next, we will check how well the MARS spatial photon distribution corresponds to analytical estimates.

The primary, high-energy reactions that lead to GB and bremsstrahlung from lost beam electrons (scattered or “secondary” bremsstrahlung) are shown in Figure 1. The Feynman diagrams, taken from Nelson [10], show that bremsstrahlung and pair production are essentially the same process, with the shaded area highlighting the difference; i.e., time reversal of the input channel. In the background gas of the storage ring (SR) vacuum vessel, the bremsstrahlung (left) reaction is by far the most probable; however, once the GB photon strikes a denser medium, pair production (materialization) and subsequent bremsstrahlung can occur with almost equal likelihood to create an electromagnetic shower. Initially, the shower is composed almost entirely of photons, electrons, and positrons. The initial GB radiation generated in the “thin-target” of an ID straight section will consist only of photons. The few electrons and positrons produced are removed by the next downstream bending magnet.

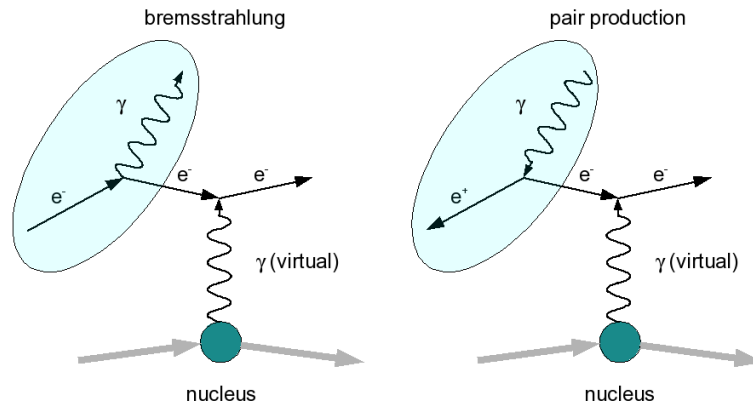


Figure 1: Feynman diagrams of the bremsstrahlung and pair production processes.

2.1 Gas Bremsstrahlung Power

Radiation from the APS SR electron beam escapes from the shielded tunnel enclosure through the production of GB photons. Multiple steps are taken to absorb this radiation to prevent the exposure of beamline personnel; these steps include the use of collimators, beam stops, and shielding. The GB is essentially thin-target bremsstrahlung radiation [11], where the primary particle (electron) trajectories are only slightly perturbed in their interaction with the medium through which they pass. The generation rate of GB photons from the passage of a high-energy electron through a background gas as function of photon energy, k , can be expressed as [10,12,13],

$$F(k)dk = 4\alpha r_e^2 \frac{N_A}{A} Z(Z+1) \frac{dk}{k} f(\nu, Z), \quad (1)$$

where $F(k)dk$ is the number of photons generated per $\text{g}\cdot\text{cm}^{-2}$ of gas length in the energy interval between k and $k+dk$ MeV, the fine structure constant, $\alpha=1/137$, the classical electron radius, $r_e=2.83\times 10^{-13}$ cm, A is the atomic mass, Z is the atomic number of the medium, and the form factor, f [14,15], can be given as,

$$f(\nu, Z) = \left\{ \left[\nu^2 - \frac{4}{3}\nu + \frac{4}{3} \right] \ln \left(\frac{183}{Z^{1/3}} \right) + \frac{1}{9}(1-\nu) \right\}, \quad (2)$$

where $\nu=k/E_T$, and E_T is the initial energy of the electron ($E_T=7$ GeV). The radiative linear stopping power in units of MeV cm^{-1} is closely related to Eq.(1),

$$\begin{aligned} \left. \frac{dT}{dx} \right|_{\text{rad}} &= -4\alpha r_e^2 \frac{N_A}{A} Z(Z+1) T \int_0^1 \frac{d\nu}{\nu} f(\nu, Z) \rho \\ &= -4\alpha r_e^2 \frac{N_A}{A} Z(Z+1) \left[\ln \left(\frac{183}{Z^{1/3}} \right) + \frac{1}{18} \right] \rho T \\ &= -\frac{\rho T}{X_o}, \end{aligned} \quad (3)$$

where T is the electron kinetic energy in MeV and ρ is the mass density of the medium; in this regime, $T \approx E_T$, the total electron energy ($E_T=T+E_o$, where $E_o=mc^2$). Equation (3) is the result of integrating the high-energy cross section for complete screening of the nucleus. The radiation length is identified in Eq.(3) as,

$$X_o^{-1} = 4\alpha r_e^2 \frac{N_A}{A} Z(Z+1) \left[\ln \left(\frac{183}{Z^{1/3}} \right) + \frac{1}{18} \right], \quad (4)$$

where X_o is expressed in units of g/cm^2 . Tsai [16] and Yao et al. [17] express the radiation length slightly differently but with virtually the same numerical results. The

effective atomic mass of a gas mixture, such as air, is defined as a sum of the weighted molar fractions of the atomic mass of each component in the mixture,

$$A^* = \sum_i f_i A_i . \quad (5)$$

The main constituents of dry air are given in Table 1; for these values $A^*=14.66$ g/mole. In a manner similar to that given by Eq.(5), the effective atomic number for air is determined as $Z_{\text{eff}}=7.31$. Given A^* and Z_{eff} , the radiation length for air is found to be 37.06 g/cm². According to the Particle Data Group [18], the radiation length for dry air is 36.65 g/cm². In MARS, effective mass is not used, rather the Bragg additivity rule is applied [19] where the effective linear stopping power, $\langle dE/dx \rangle = \sum w_j (dE/dx)_j$, where w_j represents the weighting fraction of element j . High-energy electrons will interact with the electrons and nucleus of individual atoms, not collectively with the molecules. Molecular binding energy is weak and can therefore be ignored. Alternate forms of Eq.(1) are given in the literature [14,20]; however, care must be exercised when taking account of the atomic weight of the gas mixture.

Table 1: Molar fractions for the main components of dry air

Component	Molar fraction	Atomic mass, A (g/mole)	Atomic Number Z
N (N ₂)	0.7808	14.007	7
O (O ₂)	0.2095	15.999	8
Ar	0.0093	39.948	18

Equation (3) expresses the photon energy loss per electron per cm in a standard atmosphere and provides a convenient way to calculate the GB power. For the thin-target case, where $x \ll X_0$, the energy radiated by an electron is just the product of the electron kinetic energy and the ratio of path length to radiation length. The total GB power may be written as,

$$P_\gamma = 1.7 \times 10^{18} \frac{pI}{T_K} \frac{\rho}{X_0} L_{ss} T \frac{\text{MeV}}{s}, \quad (6)$$

where I is the stored beam current in mA, p is the residual gas pressure in Torr, T_K is the residual gas temperature in Kelvin, and L_{ss} is the total length of the straight section in cm. The total GB power per mA from 7 GeV electrons in a residual background gas pressure of 1 nTorr air at 293K (20°C) is 4.6×10^{-7} W for a straight section length of 1538 cm. For all temperature-dependent calculations made here, it is assumed $T_K=293$ K (20°C). The density of dry air at 293K and 760 Torr (101.325 kPa) is 1.205×10^{-3} g/cm³.

The functional form defined by Eq.(2), varies slowly with electron energy for the main constituents of dry air, as shown in Figure 2. The form factor is given as a function of photon energy, k . Equation (1) is valid for photon energies up to T and is zero above T . The GB spectra derived from Eq. (1) for 7 GeV electrons traveling through hydrogen, nitrogen, oxygen, and argon backgrounds, normalized to 1 nT and 1 mA, are presented in Figure 3. Residual gas analysis (RGA) studies of gas composition in APS insertion

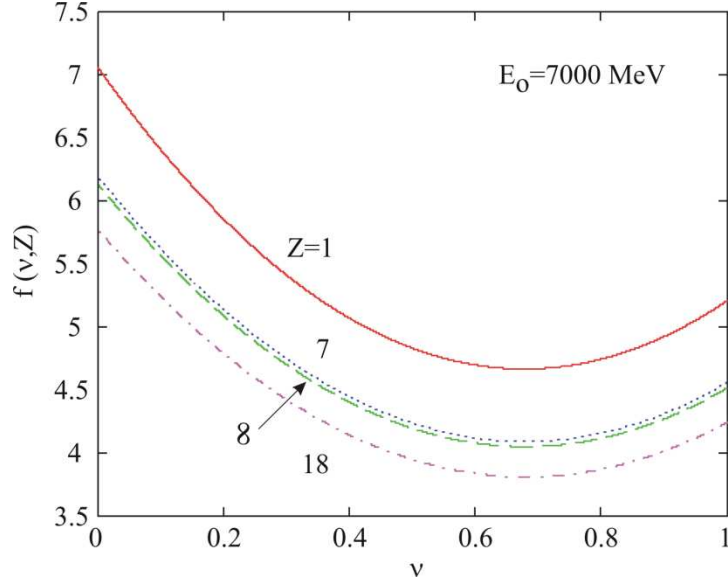


Figure 2: Gas bremsstrahlung form factor (Eq.(2)) for H ($Z=1$), N ($Z=7$), O ($Z=8$), and Ar ($Z=18$).

device (ID) beamlines 6 and 11 indicated Z_{eff} values of 4.08 and 3.18 [5,6]. A comparison of normalized GB spectra for ID beamlines 6 and 11 are compared with air ($Z_{\text{eff}}=7.31$) in Figure 4. These figures show how GB power varies with the atomic number of elemental gases and what might be expected from specific beamlines based on measured Z_{eff} values. Ignoring the effects of the form factor given by Eq.(2), Eq.(1) shows that normalized GB power scales with Z_{eff} approximately as,

$$\frac{P(Z_{\text{eff}1})}{P(Z_{\text{eff}2})} \approx \frac{Z_{\text{eff}1}^2 + Z_{\text{eff}1}}{Z_{\text{eff}2}^2 + Z_{\text{eff}2}}. \quad (7)$$

Using Eqs.(1) and (2), total GB power levels can be estimated. Analytical results are compared to simulations with MARS, as well as to measured levels in specific APS beamlines. A comparison of GB power levels, normalized to 1 nT and 1 mA are given in Table 2. The MARS result is approximately 2 percent less than the analytical value; however, the measured GB power levels are lower by factors of 3-20. The MARS power calculation is based on integrated spectral fluence in a tally volume just downstream of the source and is discussed in greater detail below. Possible explanations for the differences between measured and predicted GB power levels are presented in Section 4.

Analytical GB power estimates are not given in Ref. 9 or 21. A semi-empirical dose prediction based on a fluence-to-dose conversion factor given by Franck [22][†] is provided, as discussed below. The GB power level suggested by the form used in LS-260 [9] comes from Rindi [14], but its quantity is only partially provided. An estimated level of 1.2×10^5 photons per second is mentioned for the beamlines in Refs. 9 and 21, but no power calculation is offered. For example, a simple estimate can be made by taking

[†] The author is indebted to ANL Librarian M. Straka for her diligence locating this reference.

Table 2: Comparison of measured, predicted, and simulated normalized GB power.

	Z_{eff}	$P_{\gamma,\text{meas}}[5,9,23,21]$ (W/nTorr/mA)	Analytic, Eq.(6) (W/nTorr/mA)	MARS, Eq. (13) (W/nTorr/mA)
Air	7.3	(1.0×10^{-7})	4.59×10^{-7}	4.33×10^{-7}
6-ID e^-	4.08	$0.6 \pm 0.03 \times 10^{-8}$	1.64×10^{-7}	* 1.48×10^{-7}
10-ID e^+	4.6	1.0×10^{-8}	2.02×10^{-7}	* 1.84×10^{-7}
11-ID e^-	3.18	$1.9 \pm 0.14 \times 10^{-8\dagger}$	1.06×10^{-7}	* 0.95×10^{-7}
12-ID e^-	4.6	1.5×10^{-8}	2.02×10^{-7}	* 1.84×10^{-7}
12-ID e^+	4.6	2.4×10^{-8}	2.02×10^{-7}	* 1.84×10^{-7}
13-ID e^+	4.6	4.8×10^{-8}	2.02×10^{-7}	* 1.84×10^{-7}
15-ID	4.6	0.7×10^{-8}	2.02×10^{-7}	* 1.84×10^{-7}

* MARS air result scaled with Z_{eff} .

† Given incorrectly as 2.9×10^{-8} W/nTorr/mA in Ref. 6.

the product of the photon rate with the average photon energy; however, the average photon energy is not given, nor are the conditions for which the photon rate estimate is made (current or pressure). As discussed below, the average photon energy determined from the analytical GB spectral distribution is found to be 531 MeV. Assuming the estimated photon rate is made for 100 mA operation in an air background of 1 nTorr, the normalized GB power is 1.0×10^{-7} W/nTorr/mA. The estimated level is roughly a factor of 4 times lower than the analytical result presented in Table 2; this discrepancy is also noted by Asano et al. [24]

Assessing background pressure and composition in the SR straight sections is vital if one wishes to accurately model the production of GB; especially in the low-conductance undulator vacuum chambers. Berkvens and coworkers [25] at the ESRF have developed a Monte Carlo analysis in an effort to address this problem, and it may be useful to adapt

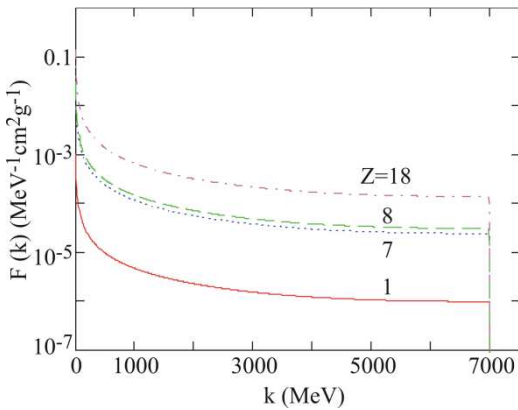


Figure 3: GB spectral density from Eq.(1) for air components N ($Z=7$), O ($Z=8$), and Ar ($Z=18$) and H ($Z=1$).

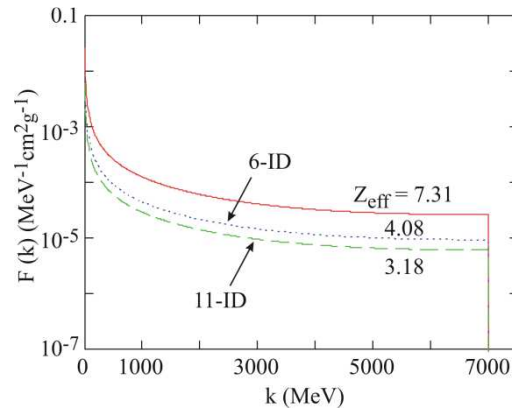


Figure 4: GB for Z_{eff} of air (N, O, and Ar), as well as residual gas in 6-ID and 11-ID straight sections.

this program for the APS. This would add a level of accuracy to both the simulated and analytical estimates of GB by characterizing the pressure at the source of the radiation. One may still need to provide the components of the background gas (i.e., Z_{eff}), however.

2.2 Pair Production

As shown in Fig. 1, GB and pair production are essentially the same process. The GB will dominate in the low density of the straight section background gas. In the straight section, pair production can only occur after the GB photons have been created. The density of the GB photons created in the straight section is low; therefore the further generation of pair production electrons and positrons, which depends on the density of both the GB photons and the background gas atoms, is extremely low. However, once the GB photons strike a dense medium, such as a beam stop, shutter, or the vacuum chamber wall, then pair production and the subsequent shower of photons, electrons, and positrons can take place. Each subsequent generation increases the number of shower constituents and lowers the average energy until the critical energy is reached. The critical energy is defined by Rossi as the energy where radiation losses (GB and pair production) are approximately equal to the collision losses of electrons (ionization)[26]. The differential cross section for pair production with respect to energy may be written as [17],

$$\frac{d\sigma}{dv} = \frac{A}{X_o N_A} \left(1 - \frac{4}{3} v(1-v) \right). \quad (8)$$

Integrating over the normalized energy, the total cross section is

$$\begin{aligned} \sigma_T &= \frac{A}{X_o N_A} \int_0^1 dv \left(1 - \frac{4}{3} v(1-v) \right) \\ &= \frac{7}{9} \frac{A}{X_o N_A}. \end{aligned} \quad (9)$$

For air, $\sigma_T = 5 \times 10^{-25} \text{cm}^2$. The pair production rate may be expressed as,

$$R_{pp}(z) = n_{ss} n_{\gamma}(z) \sigma_T c, \quad (10)$$

where n_{ss} is the gas density and $n_{\gamma}(z)$ is the photon density in the straight section and c is the speed of light. We expect that the density of photons grows linearly with distance in the straight section; therefore the rate of pair-produced electrons and positrons will grow quadratically with length. Based on photon production from Eqs.(1) and (2), the total rate of pair production from a 1538-cm-length straight section is $\dot{N}_{pp} = 1.1 \times 10^{-9} \text{s}^{-1} \text{mA}^{-1} \text{nTorr}^{-1}$. Thus, even at 300 mA, the rate of pair production in the straight section is very low. A more probable event is a second scattering of the original electron; however, even this rate will be small because the target is so thin. Pair

production does play an important role in the generation of the electromagnetic shower created after GB photons strike a dense object, such as a collimator or beam stop.

2.3 Gas Bremsstrahlung Dose Estimate

MARS and other programs can calculate GB dose accurately through Monte Carlo simulations. Here we will cover an approach where simulation is used to generate the GB spectral fluence, then the absorbed dose in a tissue-equivalent phantom is estimated manually with fluence-to-dose conversion factors. With the power of present day computers, there is no longer a reason to perform a manual calculation, as this only reduces the accuracy of the result; however, it is important to test and verify computer simulation output when possible. We follow this method in the present section to understand previously published results, which are the only data to which we can compare MARS. The estimate does not include dose from synchrotron x-rays. Using fluence-to-dose conversion factors provided by Rogers [27], an estimate of maximum GB dose can be calculated once the photon spectral fluence is obtained by simulation, or, as an approximation, the flux and average photon energy are known. The maximum dose is an estimate of what a person would receive from GB radiation if standing in the beam for a given time within the FOE, without any shielding present. Later in Section 3, we will use MARS to show that an unshielded tissue phantom, 30 cm in depth, receives the maximum dose-rate from 7 GeV GB at 30 cm.

The GB photon spectral fluence (SPG) predicted by MARS for 300 mA, 7 GeV electrons striking a 24-cm-length, 1 atmosphere (760 Torr, $\rho_{\text{air}}=0.001205\text{g/cm}^3$) air target is shown in Figure 5. The relatively high-pressure target is employed for statistical purposes to generate sufficient photon numbers and events in downstream geometries of interest; the results are then scaled to the actual vacuum chamber pressure and length. The primary electron beam is assumed to be a point source with zero divergence. The log-log scale in Figure 5b shows the low-energy photon distribution more clearly. The total photon fluence rate is determined by integrating SPG data over the energy range and multiplying this result with the cross-sectional area of the volume in which the photon

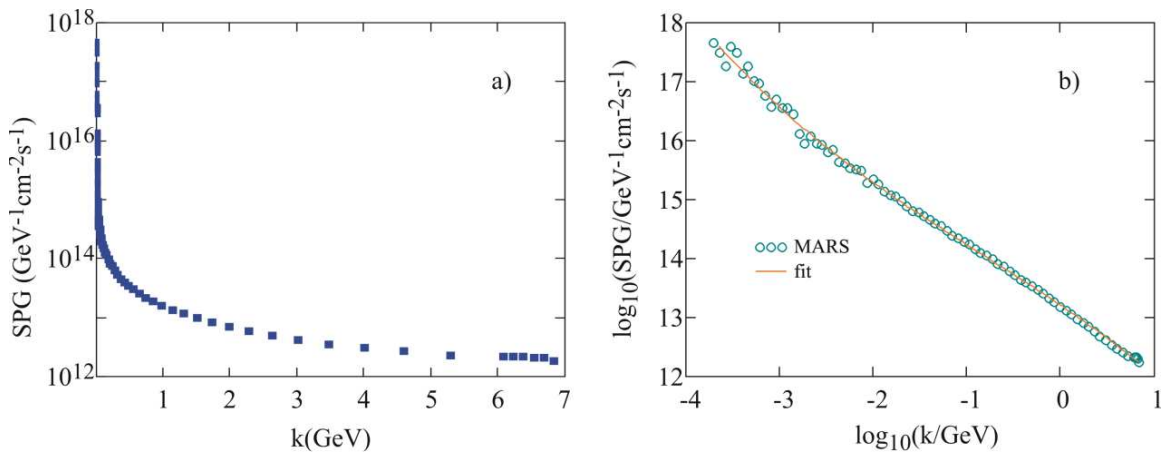


Figure 5: MARS GB photon spectral fluence rate (SPG) on a) semi-log and b) log-log scales.

spectrum is tallied. Integrating spectral fluence rate over energy yields the total photon flux, as follows,

$$\Gamma_{\gamma} = \int_0^T dk \text{SPG}(k) \approx \sum_{i=1}^{N_b} \Delta k_i \text{SPG}(k_i), \quad (11)$$

where MARS replaces the integration with a sum over the number of spectral bins, N_b . In MARS, the dose-rate from photons in a given region is determined by integrating the spectral fluence rate with the energy-dependent fluence-to-dose conversion factor, f_{ϕ} [27,28],

$$\dot{D}_{\gamma, \text{MARS}} = A_{\text{GB}} \int_{k_{\text{min}}}^{k_{\text{max}}} dk \text{SPG}(k) f_{\phi}(k) \approx A_{\text{GB}} \sum_{i=1}^{N_b} \Delta k_i \text{SPG}(k_i) f_{\phi}(k_i), \quad (12)$$

where A_{GB} is the surface area of the tally volume normal to the beam. The integration is done numerically in MARS.

Fluence-to-dose conversion factors given by Rogers are compared with those from Franck in Figure 6. The Franck data, originally given in units of Grays has been converted to Sieverts assuming a quality factor of 1.

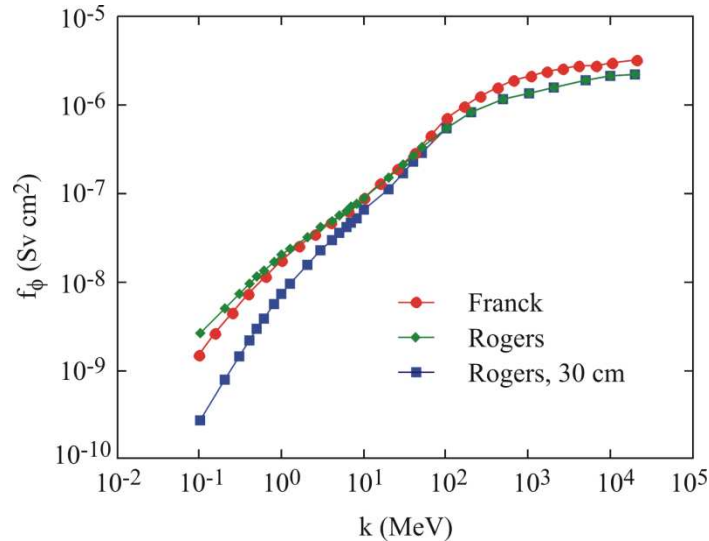


Figure 6. Fluence-to-dose conversion factors from Franck [22] and Rogers [27]. Rogers' data are presented for both a fixed depth of 30 cm, as well as at the maximum dose position in the phantom; these curves converge for photon energies above 100 MeV.

In the MARS model, GB spectral fluence rate is tallied in a vacuum region just downstream of the air target. The tally volume is a square cross section, right-rectangular prism. The GB tally volume is 10 cm in both transverse dimensions and 5 cm in depth; thus the surface area of the tally volume normal to the beam is $A_{\text{GB}}=100 \text{ cm}^2$. Electrons

and pair production positrons are removed from the beam just upstream of the tally region at the air-vacuum interface. A sketch of the MARS model, indicating the region of GB production is given in Figure 7; in this case, the FOE phantom is oriented beside the beam stop (target) for PN simulations (PN simulations are discussed in Section 4). Only a small fraction of photons entering the tally volume through the upstream surface are lost before exiting through the downstream surface. We can rewrite the normalized GB power in terms of the photon spectral fluence rate in Eq. (11) as,

$$P_{GBm} = \frac{p_{ss}}{p_{ref}} \frac{L_{ss}}{L_{ref}} A_{GB} \int dk SPG(k)k, \quad (13)$$

where we scale for the actual straight section gas pressure, p_{ss} ($=10^{-9}$ Torr), as well as the true straight section length L_{ss} ($=1538$ cm); p_{ref} and L_{ref} refer to the pressure and length of the straight section target used in the simulations. For most of the simulation data presented here, $p_{ref}=760$ Torr and $L_{ref}=24$ cm. A rough estimate of the normalized power can be expressed as,

$$P_{GBm} = \frac{p_{ss}}{p_{ref}} \frac{L_{ss}}{L_{ref}} \Gamma_{\gamma} A_{GB} \langle k_m \rangle, \quad (14)$$

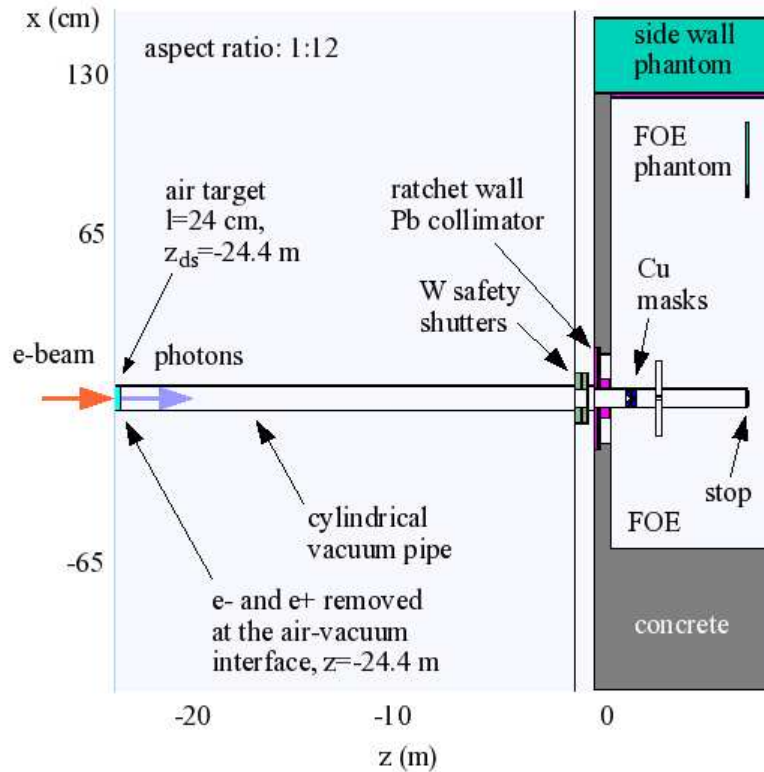


Figure 7: Sketch of the MARS air target and FOE geometry; x-z view at beam elevation. The FOE phantom is oriented beside the stop (target) for PN simulations (see Section 4).

where $\langle k_m \rangle$ is the average GB photon energy determined from the MARS spectrum,

$$\langle k_m \rangle = \frac{\int dk \text{SPG}(k)k}{\int dk \text{SPG}(k)}. \quad (15)$$

For the GB spectral fluence distribution shown in Fig. 5, over the energy range of 0.2 MeV to 7000 MeV, $\langle k_m \rangle = 356$ MeV.

Though we seek the dose, it is important to know the power for both comparison and calibration of models. The result of numerically integrating Eq.(13) is given in Table 2. We now estimate the dose-rate. Using energy-dependent fluence-to-dose conversion factors published by Rogers and plotted in Figure 6, the dose-rate in 1 cm² at 300 mA and 1 nTorr is found to be 0.609 Sv/hr. The values of $f_\phi(k)$ were determined by polynomial fitting the Rogers data [27] at a phantom depth of 30 cm. Using the conversion factors provided by Franck with the MARS spectral fluence rate data yields a dose-rate of 1.175 Sv/hr.

The analytical dose-rate can be determined in largely the same manner; however, the analytical spectrum varies as 1/E, differing from that of the simulation (see Fig. 5b). MARS indicates a modest enhancement of the low-energy photon spectrum. As such, integrating over the same energy range, the average photon energy for the analytic spectrum is 531 MeV. The cross-sectional area of the tally volume is used to extract the correct power from the MARS simulations; however, for the dose-rate calculation, a cross-sectional area of 1 cm² is assumed. Incorporating the fluence-to-dose conversion factor into Eq. (3), the analytic dose-rate can be written as,

$$\dot{D}_{\text{GBa}} = 4\alpha r_e^2 \frac{N_A}{A_*} Z_{\text{eff}} (Z_{\text{eff}} + 1) \rho T \int_0^1 \frac{dv}{v} f(v, Z_{\text{eff}}) f_\phi(v). \quad (16)$$

The analytic dose-rate is found to be 0.427 Sv/hr and 0.624 Sv/hr with Rogers' and Franck's conversion factors, respectively.

A semi-empirical, total beam-integrated GB dose-rate given by Franck [22] was used to determine the source term for the EGS4 simulations presented in TB-20, to be discussed in the next section. The semi-empirical form is expressed as [2,9],

$$\dot{D}_{\text{se}} = \frac{f_{\phi,\text{eff}} \dot{N}_e L_{\text{ss}}}{\pi \theta_{\text{gb}}^2 X_o L(L + L_{\text{ss}})}, \quad (17)$$

where $f_{\phi,\text{eff}}$ is the effective fluence rate-to-dose-rate conversion ratio for bremsstrahlung photons [22] ($f_{\phi,\text{eff}} = 3 \times 10^{-6}$ Gy/hr/ ϕ), \dot{N}_e is the number of electrons per second (300 mA = 1.873×10^{18} e/s), L_{ss} is the length of the ID straight section (1538 cm), $\theta_{\text{gb}} = 1/\gamma$ is the characteristic opening angle [29] of the radiation cone ($1/1.37 \times 10^4 = 73$ μ rad), X_o is the radiation length in air for 1 nTorr (37.1 g/cm² (760 Torr)/ 10^9 Torr/ $\rho_{\text{air}} = 2.34 \times 10^{16}$ cm), and L is the length from the end of the straight section to the observation point (2440 cm). Equation (17) provides a rate of 2.23 Sv/hr (223 rem/hr). Note that the dose-rate is

simply the product of the electron current with a single fluence-to-dose conversion factor modified by spreading of the GB radiation at the characteristic angle and assessed at a position of interest in the FOE. The fluence-to-dose conversion factor is the same one used in TB-20 (the factor is near the peak value presented in Figure 6), which corresponds to fluence rate-to-dose-rate at the highest energy. Again, no integration was done in the earlier references, only a single value was used. Asano and Sasamoto [30] also used Eq.(17) to calculate dose-rates for beamlines at SPring-8. Further discussion of fluence-to-dose conversion factors, also known as response functions, is provided by Shultis and Faw [31].

A comparison of initial maximum dose-rates is given in Table 3. In the table, four approaches are shown: 1) integrating the analytic spectrum (1/k) with the Rogers' and Franck's fluence-to-dose conversion factors; 2) integrating the MARS-generated spectrum (partial simulation result) with Roger's and Franck's fluence-to-dose factors; 3) the "semi-empirical" approach of Franck's, i.e., simply the product of the integrated flux with the fluence-to-dose conversion at the average photon energy (Franck appears to have used the maximum energy in [22] as does Job in [2]); and 4) the full MARS simulation result. For the semi-empirical approach, the integrated flux is computed by dividing the total GB power by the average photon energy over 1 cm^2 . Multiplying the integrated flux by Roger's fluence-to-dose conversion factors at the average energy, the respective maximum dose-rates are 2.24 Sv/hr using MARS spectral fluence to derive the total GB power and 1.73 Sv/hr using the analytical spectrum. These estimates are clearly conservative. The dose-rate labeled "Full MARS" is determined directly from simulation output (correcting for pressure and target length). MARS uses ICRP 51 (Rogers' data) for fluence-to-dose conversion factors.

Table 3: Initial maximum dose-rates in a 1 cm cube phantom volume. Under the semi-empirical heading (A) refers to analytical spectrum and (M) to MARS spectrum.

Method	Analytic source	MARS spectral fluence rate	Semi-empirical	Full MARS
\dot{D}_{Rogers} (Sv/hr)	0.427	0.609	1.73 (A), 2.24 (M)	0.761
\dot{D}_{Franck} (Sv/hr)	0.624	1.175	2.23	—

With the exception of the semi-empirical Franck result, the dose-rates given in Table 3 were made assuming a scoring surface area of 1 cm^2 ; however, the distance between the source and scoring location is not involved in the estimate. Ferrari and coworkers [32] have shown the importance of scoring (detector) size when calculating dose as illustrated in Figure 1 of Ref. [32]. They have shown experimentally that as one moves close to the source, the transverse extent of the GB radiation becomes smaller than that of the detector. No increase in radiation is observed as one moves the detector still closer to the source; the same amount of total power is being intercepted. This is the condition for a 1 cm^2 detector located 31 m downstream of the center of the straight section. In general, the scoring area must be determined based on the footprint of the radiation at the detector.

2.4 Gas Bremsstrahlung Beam Distribution

It is generally thought that the GB radiation transverse distribution is roughly Gaussian with a characteristic divergence of $1/\gamma$, where $\gamma=1+T/E_0=1.37 \times 10^4$. The goals of this section are to show that a) finite transverse emittance and hence finite beam size limit the maximum intensity of the dose-rate and b) the extended length of the GB target, i.e., the vacuum chamber straight section, cause the transverse GB profile to be peaked.

The dose-rate given in Eq.(17), is described by Asano and Sasamoto [30] as providing the average dose-rate “without considering the size dependence of dose for narrow beam[s].” In addition, the fluence-to-dose tables provided by Rogers also assume a broad, parallel beam. A form similar to Eq.(17) is also used by Ferrari et al.[32] Because of the singularity as one approaches the end of the straight section, Eq.(17) is not useful for examining the dose-rate in this region. Thus one must convolve the phase space distribution of the e-beam with GB γ production resulting in a broadened γ distribution. Here we provide a simple model of flux and dose generation and the manner in which the transverse distribution varies depending on the spreading angle ($1/\gamma$) and the length of the straight section (target). This simple model removes the singularity of Eq.(17).

The size of the GB radiation can be no smaller than the beam that creates it. Betatron motion in the e⁻ beam and GB emission are essentially independent processes; therefore, the size contribution from each can be added in quadrature. The characteristic angle of the GB emission, $\theta_{gb}=1/\gamma=73 \mu\text{rad}$, is much larger than that of the beam, $x'_{\text{max}}(z) \leq 35 \mu\text{rad}$ [33]; thus, the beam divergence does not add significantly to the divergence of the GB radiation.

For simplicity, we assume a K-V [34] distribution for the electron beam, and that the beam possesses a constant, round cross section of radius $R=(\epsilon_0\beta_0)^{1/2}$, where ϵ is the beam emittance ($\epsilon_x=\epsilon_y=\epsilon_0$) and β is the betatron function ($\beta(z)=\beta_0$). The differential GB radiation dose-rate as a function of photon energy and position in the gas target can be expressed as,

$$\frac{dD_r(z)}{dz} = \int_0^T dk f_\phi(k) \Phi_\gamma(k, z) \approx f_\phi(\langle k \rangle) \frac{E_\gamma(z)}{\langle k \rangle} \frac{I}{eA(z)}, \quad (18)$$

where $\Phi_\gamma(k, z)$ represents the z-dependent GB spectral fluence rate, $E_\gamma(z)$ the total photon energy production per unit length per electron (assumed to be constant here), $\langle k \rangle$ is the average photon energy, and $A(z)=\pi r_t^2(z)$, with

$$r_t^2(z) = [\theta_{gb}(Z-z)]^2 + R^2. \quad (19)$$

In Eq.(19), z is the location of the axial slice, dz, and Z is an observation point, where $Z > z$. We again assume a constant fluence-to-dose conversion factor to simplify the problem, and that the transverse GB dose-rate profile remains a disk even though the electron and photon distributions are combined by convolution. Using E_γ determined from Eq. 3, the on-axis dose-rate for $Z < L_{ss}$ can be written as,

$$D_r(Z) = \frac{f_\phi(\langle k \rangle)}{\langle k \rangle} \frac{I}{\pi e X_o} \frac{\rho T}{X_o} \int_0^Z \frac{dz'}{r_t^2(z')} = \frac{f_\phi(\langle k \rangle)}{\langle k \rangle} \frac{I}{\pi e X_o} \frac{\rho T}{X_o} \left(\frac{1}{R\theta_{gb}} \right) \tan^{-1} \left(\frac{\theta_{gb} Z}{R} \right). \quad (20)$$

We define $z_b=R/\theta_{gb}$ as the distance in the straight section where the radius of the GB radiation is equal to the rms width of the beam. In the limit where $z \ll z_b$, the dose-rate increases linearly with z ; that is, the dose-rate grows at a constant rate along the column of residual gas. In the opposite case where $z \gg z_b$, the dose-rate saturates,

$$D_{rsat} = \lim_{\substack{z \rightarrow \infty \\ Z \leq L_{ss}}} D_r(z) \approx \frac{f_\phi(\langle k \rangle)}{\langle k \rangle} \frac{I}{\pi e X_o} \frac{\rho T}{2R\theta_{gb}}. \quad (21)$$

Note that in the former situation, θ_{gb} drops out of the expression (not shown); this makes sense physically, since for a short target, it is just the extent of the electron beam that determines the transverse size of the GB. More detailed beam profiles can be addressed in future analyses. For the present, we assume $R=275 \mu\text{m}$ [33]. The target length is normalized by the distance required to produce a transverse size in the GB beam equal to that of the electron beam, then $z_b=275 \mu\text{m}/73 \mu\text{rad} = 3.77 \text{ m}$ and the length of an ID straight section is $4.08z_b$. The saturated dose-rate for 300 mA of 7 GeV electrons in 1 nTorr air is calculated from Eq. (21) to be 305 Sv/hr; the Roger's fluence-to-dose conversion factor is $3.2 \times 10^{-10} \text{ Sv}\cdot\text{cm}^2$ at an average photon energy of 531 MeV. The saturated dose-rate is indicated in Figures 8a and b. Figure 8a shows a linear increase in dose-rate initially along the straight section length followed by an asymptotic behavior.

The radial distribution can be constructed in a piece-wise continuous manner. Combining Eqs. (18), (19), and (20), for $Z \leq L_{ss}$ and $R \leq r_i < r_t$ we can numerically integrate to find the dose-rate distribution as a function of radius as follows,

$$D_r(r_i) = 2R\theta_{gb} D_{rsat} \frac{\Delta Z}{\pi} \sum_{j=0}^{N-i} \frac{1}{(r_{tN-j})^2}. \quad (22)$$

For $r_i < R$, the dose-rate is constant and is given by Eq.(20); for $r_i \geq (R^2 + Z^2 \theta_{gb}^2)^{1/2}$, $D_r(r_i)=0$. Radial GB distributions for $Z < L_{ss}$ are presented in Fig. 8b. The integration ends at $N_{max}=L_{ss}/\Delta z$; for $\Delta z=1 \text{ cm}$, $N_{max}=1538$. Beyond the straight section where $Z > L_{ss}$, the electron beam has been bent out of the path of the GB. Assuming no losses, the total GB radiation energy is now constant with Z . The radius of constant dose-rate expands as $(R^2 + [(Z-L_{ss})\theta_{gb}]^2)^{1/2}$, and the intensity now drops. As Z increases, the radial profile begins to flatten as the ratio of L_{ss} to Z becomes small. The maximum dose-rate in a hutch 31 m downstream from the center of the straight section falls to 12.3 Sv/hr as the GB beam spreads to a FWHM radius of 2.14 mm. The FWHM dose-rate in 1 cc at the hutch location is 1.77 Sv/hr in good agreement with the semi-empirical analytical result presented in Table 3 using Rogers data. Radial dose-rate profiles based on this simple uniform beam model at $z=31 \text{ m}$ and 38 m from the center of the straight section are presented in Fig. 8c.

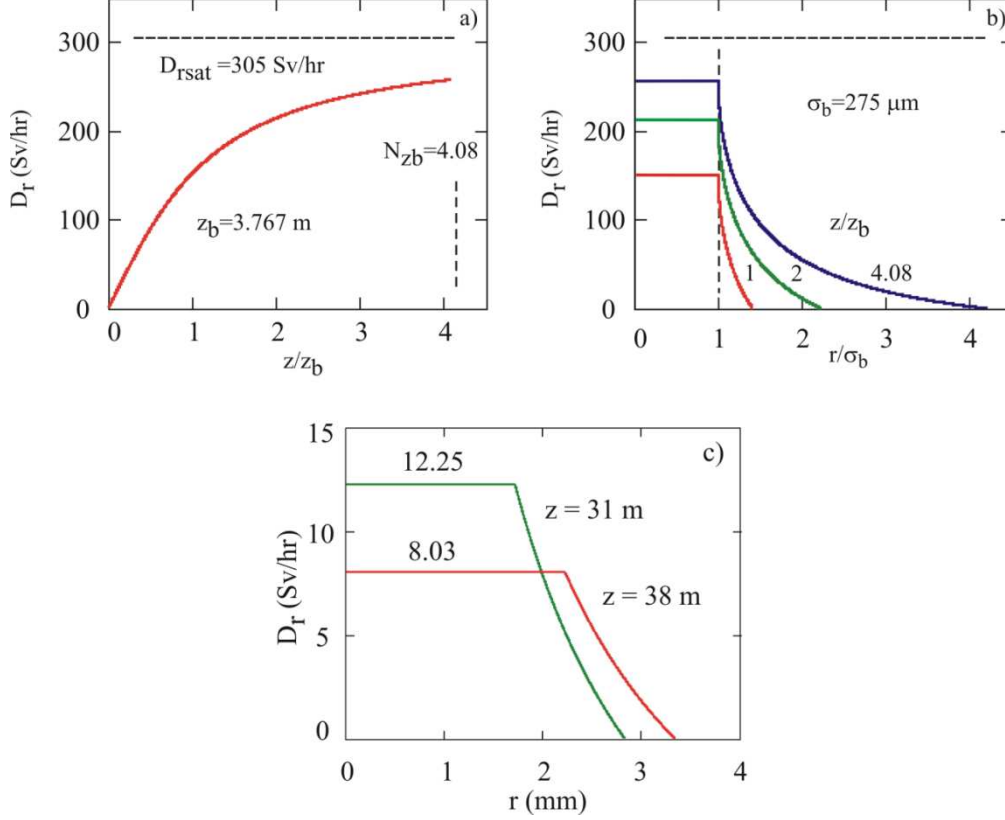


Figure 8: a) GB peak dose-rate from Eq. 20; b) dose-rate radial profiles within an ID straight section; and c) radial dose-rate profiles at $z=31$ m and 38 m downstream from the center of a straight section.

The point of this simple model is to show how the GB profile spreads from a longitudinally extended source. The discussion here also indicates that the singularity in Eq.(17) has been removed. The fact that GB beam transverse profiles are dependent on the electron beam transverse distributions may have applications for beam diagnostics.

The transverse spatial distribution of GB radiation generated by MARS at the location of a beam stop, 31 m downstream of the center of the undulator straight section is presented in Figure 9. The gamma fluence rate (FLG, units: $\text{cm}^{-2}\text{s}^{-1}$), shown in Fig. 9, represents the average of 10 separate simulations where 2×10^8 events are used to model the primary 300-mA, 7-GeV electron beam. The radial distribution presented in Fig.9 is fit to the form,

$$f_f(r, z) = A_r(z) \exp\left[-\frac{r^2}{r_{e1}(z)}\right] + B_r(z) \exp\left[-\frac{r^2}{r_{e2}(z)}\right]. \quad (23)$$

The double Gaussian function is not meant to imply specific physical mechanisms, but is simply employed to fit the simulation data. This function fails at higher radii; however, near the center of the GB the fit is good. The fit parameters are given in Table 4. The angular distribution of photons is determined by binning into the i^{th} element,

$$G_{\Omega_i} = \frac{2\pi \left[(i+1) \Delta r^2 \right] \sum_j \sum_k \phi_{k,j} \delta(N_{k,j} - i)}{K \Delta \Omega_i \sum_j \sum_k \delta(N_{k,j} - i)}, \quad (24)$$

where $\phi_{j,k}$ is the MARS fluence rate data in voxel j,k , $N_{j,k}$ is the x-y histogram position index, δ is the Kronecker delta, and K is a scaling factor. $\Delta \Omega_i$ is the differential solid angle, defined as,

$$\Delta \Omega_i = 2\pi \sin(\theta_i) \Delta \theta, \quad (25)$$

where $\theta_i = r_i / (L_{ss}/2 + L)$ and $\Delta \theta = \Delta r / (L_{ss}/2 + L)$. The distribution is arbitrarily normalized to G_{Ω_0} .

Table 4: Normalized double Gaussian fit to the radial profile presented in Figure 9.

$G_{\Omega_0}(\text{sr}^{-1} \text{e}^{-1} \text{m}^{-1}, 1 \text{ nTorr})$	A_r	r_{e1} (cm)	B_r	r_{e2} (cm)
3.359×10^{-6}	0.514	0.701	0.365	1.680

The photon fluence rate is recorded in a 5 cm by 5 cm x-y histogram region 1 cm thick in the direction of the beam, centered on the beam axis. The region is divided into a histogram array 250×250 in x- and y-directions. The photon fluence rate is tallied for each “voxel” or volume element of the fluence histogram. The transverse dimension of each voxel is then 0.2 mm by 0.2 mm. The fluence histogram volume is not to be confused with the right-rectangular prism vacuum volume mentioned earlier, where the spectral fluence rate was recorded.

One must use care when specifying the dimensions of the histogram and voxels. Summing together a large region to reduce noise in the simulation may lead to a GB width significantly broadened by the size of the “detector.” The resulting profile will be the convolution of the detector size and of the GB distribution. For example, a histogram region 2 mm in width will broaden the GB profile presented in Fig. 9 from 1.78 to 2.54 mm. The beam half-width at half-maximum (HWHM) is in reasonable agreement with the opening angle approximation $L\theta_{gb} = 1.70$ mm from the downstream end of the straight section ($L = 23.3$ m). Past attempts to measure the transverse distribution used thermoluminescent dosimeters embedded within a tissue equivalent phantom [23,35]; however, the transverse size of the detectors was $3 \times 3 \text{ mm}^2$, and spacing was varied between 3 and 5 mm. Though the distributions were shown to be peaked, it is difficult to assess the actual beam profiles. The y-distribution in Fig. 9 is generated using a double Gaussian fit of the radial data collected in x-y gamma fluence histograms.

A GB air target 24 centimeters in length at a pressure of 1 atm is approaching a thick target; the air column target density is $2.89 \times 10^{-2} \text{ g/cm}^2$. To this end, we would like to know if the air target specified leads to an accurate description of the photon beam or if multiple scattering broadens the distribution. A comparison of three GB target

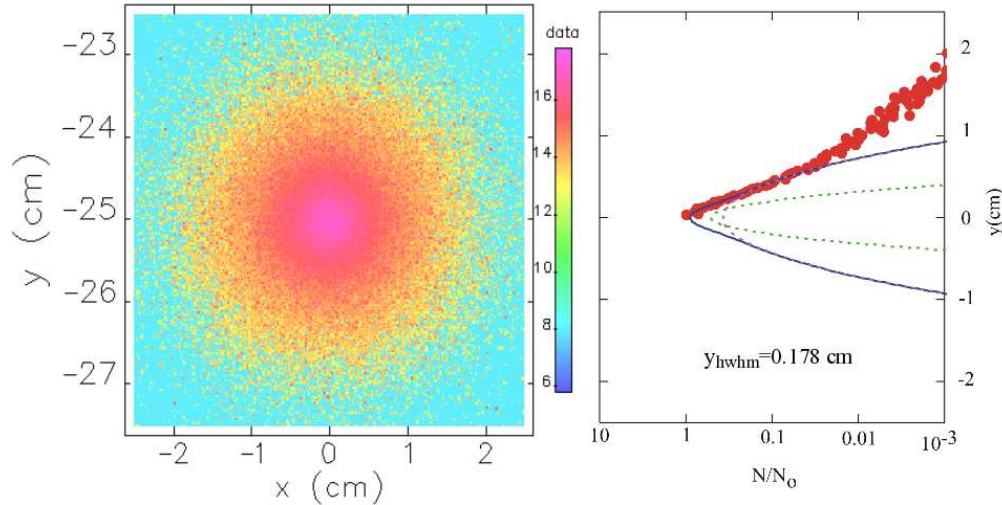


Figure 9: MARS GB photon fluence (uncorrected), radial simulation data, and y-profile using a double Gaussian fit of the radial data 31 m downstream from the air target. Using a 24 cm, 1 atm air target ($\rho L = 0.0289 \text{ g/cm}^2$).

densities are presented in Figure 10. Target densities of $1.2 \times 10^{-2} \text{ g/cm}^2$ or less have been recommended by Asano [36]; however, as shown in Fig. 10, a density of $2.89 \times 10^{-2} \text{ g/cm}^2$ closely matches this recommendation. For additional studies presented in this document, a target density of $2.89 \times 10^{-2} \text{ g/cm}^2$ is employed, unless otherwise noted. Further discussion of the GB target and comparisons with other target densities as well other code results are given in Appendix A.

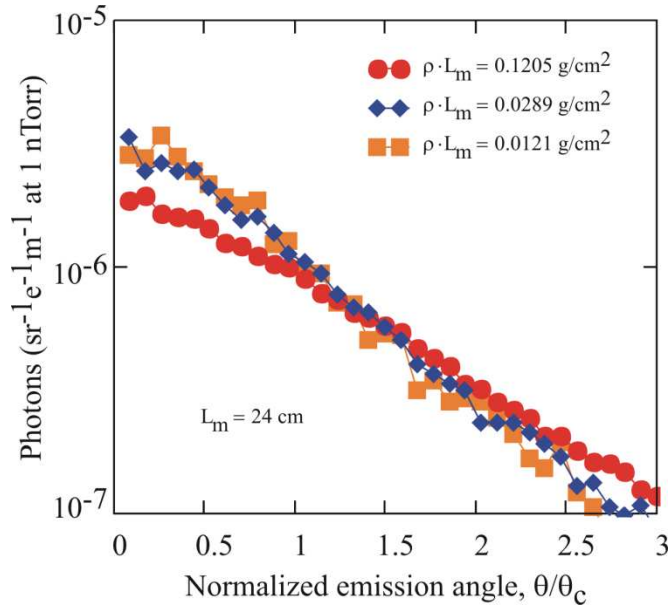


Figure 10: Comparison of GB angular distributions normalized to the characteristic angle, $\theta_c = 1/\gamma = 73 \text{ } \mu\text{rad}$ for three different target densities.

3. Contact Dose-rate—Comparison with TB-20

3.1 Description

MARS results are compared with the contact dose-rate levels reported in TB-20 [2], where simulations using EGS4 were carried out. In TB-20, the maximum dose-rate in a phantom placed behind a beam stop of variable thickness was modeled; specifically, the maximum in a 1 cm³ (cc) cube within the phantom was determined. The beam stop was irradiated by a GB beam generated in an ID straight section ($L_{ss}=1538$ cm). The beam stop material was chosen to be either lead or tungsten, and dose-rate was recorded for both cases. The EGS4 calculation did not account for the production of photoneutrons (PNs) in the target, and an arbitrary factor of 2 was used in TB-20 to include the neutron contribution to the total dose-rate.

In the MARS contact dose simulations, GB is generated in the air target described previously, placed at the center of the straight section, 31 m upstream of the beam stop. The GB radiation will include no electrons or positrons; these will all be removed by the bending magnet at the downstream end of the straight section. Other assumptions used in the contact dose simulation are 1.873×10^{18} electrons per second (300 mA) at an energy of 7.0 GeV. In the simulation, the thickness of the target shield block was varied from 1 to 30 cm. The simulation dose was recorded in a tissue phantom, 20 cm by 20 cm in transverse dimensions and 30 cm in depth, relative to the incident beam direction. The phantom geometry is divided into two regions: 1) an upstream 5×5 array composed of 4 cm by 4 cm by 5 cm x-, y-, and z-length volume elements and 2) a single 20x20x25 cm³ right rectangular prism. Though the segmentation of the phantom is chosen somewhat arbitrarily, dose was recorded in a similarly sized phantom in TB-20. Segmentation gives us the separate ability in MARS to always look at “shallow” and “deep” dose regions independently of dose histogram definitions. Also, a case was run without shielding to examine build-up factor. The simulation geometry for the case of a 20-cm-thick Pb beam stop is presented in Figure 11a. The total dose equivalent rate (DET) y-z distribution generated by the GB beam is shown in Figure 11b. MARS calculates the

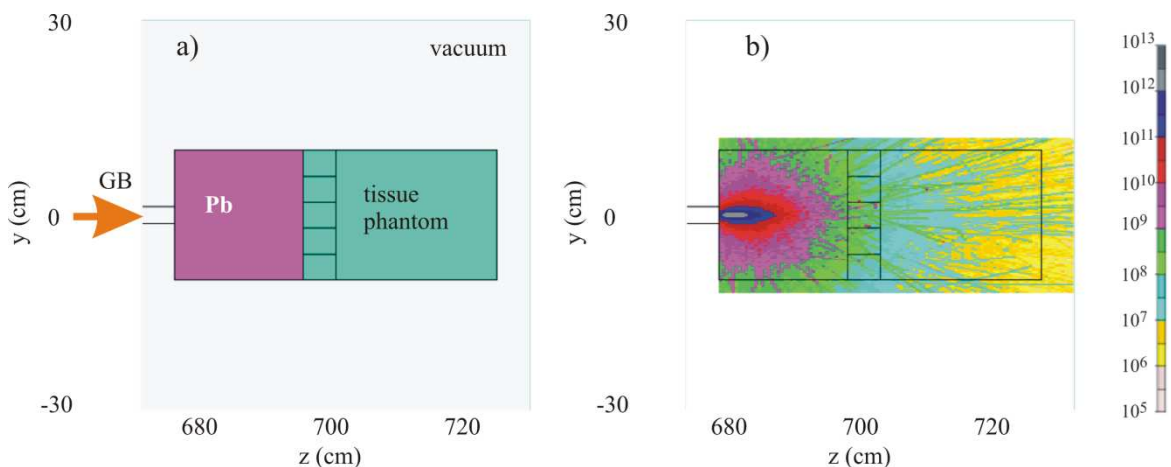


Figure 11 a) MARS contact dose geometry for a Pb stop thickness of 20 cm and b) the total dose equivalent rate distribution (DET, mSv/hr, uncorrected for pressure and length).

DET with contribution from all major radiation components including neutrons. No masks were used in these simulations.

MARS provides two methods of calculating dose or dose-equivalent: one from the geometry used to describe the model, and the other from a user-defined Cartesian grid (XYZHIS.INP) that can be placed anywhere in the same geometry. However, in the latter case, for accurate dose measurement, the grid must be positioned in the space which includes the phantom geometry defined in the GEOM.INP file. In MARS, this is called an extended geometry region; the phantom described above is an example of such a region. The histograms can be defined in multiple ways in the geometry as is done here; however, the extended geometry definition is less flexible. If it is changed, new volume regions must be redefined within the user subroutine portion of the MARS program and the program must be recompiled to produce a new executable file.

Here in one case, an x-z histogram is superimposed over the phantom volume. Data are integrated in the y-dimension in a volume divided into 100 regions in the x-direction and 120 regions in z. In the x-direction, the histogram exactly covers the phantom making the x increment, Δx , 20 cm/100=0.2 cm. In the z-direction the histogram is 60 cm in length covering phantom, beam stop and vacuum; thus $\Delta z=0.5$ cm. The integration distance is 20 cm, exactly covering the phantom.

We want to determine the maximum dose absorbed in the phantom; therefore, we must find z_{\max} , the longitudinal position in the phantom where dose is maximum. When the beam stop is removed and the phantom is unshielded, the dose maximum occurs at the deepest phantom depth; this is an example of dose buildup. However, when a stop is present, even for the minimum thickness simulated, 1cm, z_{\max} moves to the upstream end of the phantom. The former outcome is consistent with EGS simulation results reported by Rogers [27]; the latter can be explained when one considers the large number of lower energy electrons that are produced in the shower after the GB strikes a 1-cm-thick Pb or W plate. This behavior is illustrated in Figure 12, where average dose in the phantom central slice ($F(0,z)$) is shown for the no-stop case and for a Pb stop thickness of 1 cm. The vacuum upstream of the phantom in Fig. 12a represents the removal of a 30-cm heavy-metal beam stop without moving the phantom. In Fig. 12b, the phantom is moved

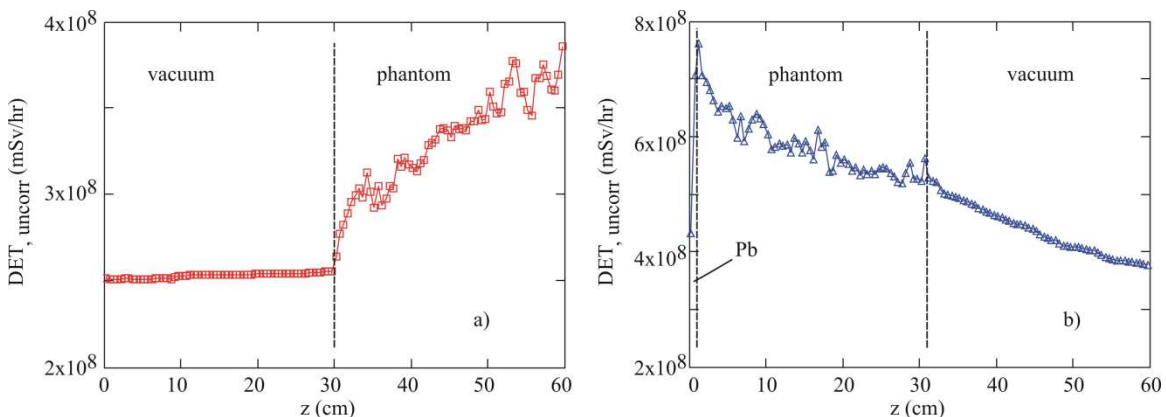


Figure 12: MARS longitudinal average dose-rate profile along the GB beam axis in a 30-cm-deep tissue phantom in the case of a) no stop and b) a 1-cm-thick Pb stop. The simulation data show the peak dose moving from downstream to upstream locations with the introduction of a beam stop. In both cases, the GB beam travels from left to right.

upstream to be in contact with the 1-cm-thick Pb slab. In Fig. 12b, the region downstream of the phantom is considered to be a vacuum. Given the data in Fig. 12, the maximum dose-rate is assumed to occur always in the phantom slice adjacent to the beam stop.

We look for the maximum dose with two sets of 2-D histograms: one as has just been described above is an x-z or y-z grid. The second grid is an x-y histogram employed to directly determine the dose in a 1-cm cube; we discuss this simulation below. We will then return to the x-z histogram and take advantage of the cylindrical symmetry of the problem to demonstrate the use of the Abel inversion technique for obtaining the maximum dose-rate.

3.2 x-y Histograms

MARS geometry can be set up to produce radial scoring; however, the cylindrical sections presently cannot be defined with an offset z-axis (that is offset transversely). A simple way around this is to define a transverse (i.e., x-y) histogram grid to score fluence or dose, as was done in the previous section, with the x- and y- midpoints of central voxel set on the axis of the GB radiation. For the present requirement, the grid need not have the high resolution employed in Section 2; instead a 21x21 grid is centered over the 20x20 cm² face of the FOE phantom. Each voxel of the grid is a 1 cc cube. The x-y histogram can then be defined at different depths in the phantom. Total dose equivalent (DET) histograms after 5 cm of beam stop thickness are presented in Figure 13 for Pb and W. The larger grid shows the positions of the geometry regions in the upstream portion of the FOE phantom; whereas, the finer grid reflects histogram data in 1 cc voxels. The DET data shown in Fig. 13 is presented on a log-10 scale and is uncorrected for pressure and target length.

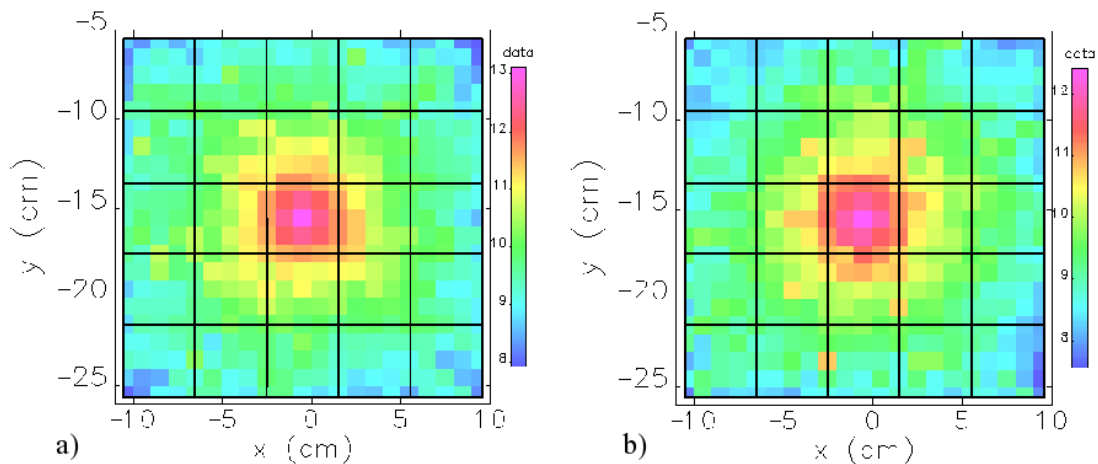


Figure 13: Total dose equivalent (DET) in the first cm of an FOE phantom after 5 cm of a) Pb and b) W. Dose is plotted using a log-10 scale. The larger grid represents the differentiation in the upstream region of the phantom; whereas, the smaller grid reflects 1 cc histogram data.

At the time TB-20 was written, giant dipole resonance (GDR) could not easily be modeled with the EGS4 program; therefore, a simple assumption was used to account for neutron dose. The assumption made in TB-20 was that half the dose from GB would be due to neutrons. Thus, no real calculation of neutrons was made in TB-20. A more comprehensive treatment of neutron production was added to EGS4 in 1995 [37]. We first compare maximum contact dose reported in TB-20 using EGS4 and results from MARS with photonuclear, GDR, and electronuclear reactions turned off in MARS. Neutron production through Bethe-Heitler muon capture in nuclei has been left on. MARS simulation results for maximum dose-rate in a 1-cc cube are presented in Figure 14. In Pb, little difference exists between dose determined with or without photon neutrons (PNs) for material depths up to 10 cm, where the shower is composed mainly of electrons, positrons, and photons. MARS results are close to the EGS4 datum at 10 cm. With W however, EGS4 results are approximately an order of magnitude higher than predicted by MARS without PNs. Agreement is also poor for 20 cm of Pb. When PNs are included, the comparison between TB-20/EGS4 and MARS is better; however, the dose from PNs dominates for Pb stop thicknesses greater than 25 cm and W thicknesses greater than 17 cm. Note that only three independent EGS4 dose-rate values exist for each beam stop material; these values are used to fit the lines shown in Fig. 14.

We next compare the dose-rate measured in a 1-cc histogram phantom volume with that recorded in an 80-cc volume defined in the GEOM.INP file. The latter volume is the central element in the upstream region of the FOE phantom; these data are presented in Figure 15. The data presented in Fig. 15 clearly show the 1-cc dose-rate is initially much higher than that in the 80-cc phantom element, as one would expect. Dose-rate in the two regions then converge for thick stops as the radiation distribution broadens. Convergence occurs in thickness greater than 20 cm in Pb and 15 cm in W. Though the 80-cc volume underestimates the dose, it predicts with reasonable accuracy the photon attenuation. This is due to the fact that, though the dose is not broad and parallel, it is fully contained within the volume of the phantom. Because of the phantom's size and the small extent of

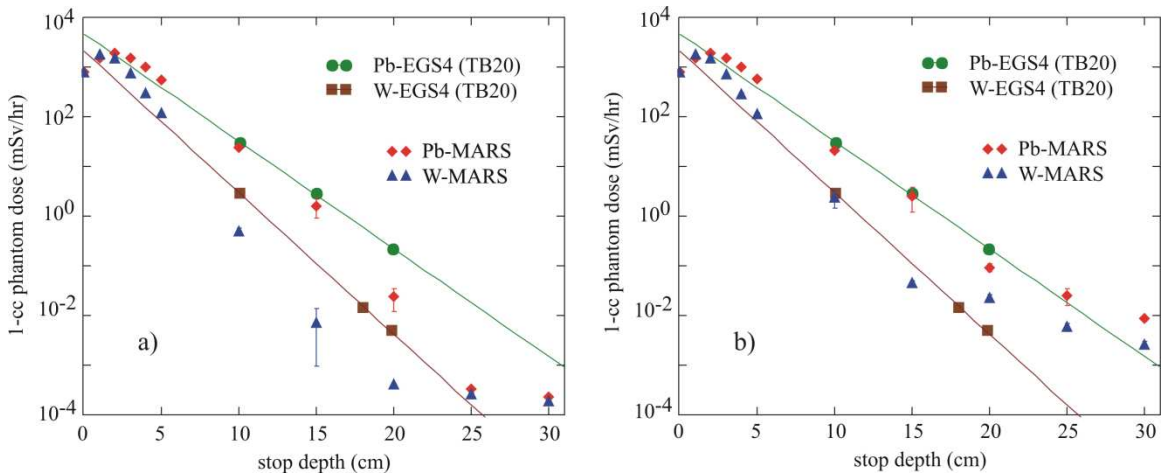


Figure 14. Maximum dose-rate determined by EGS4 and MARS in 1 cc a) without PNs in MARS and b) with PNs in MARS. (Same EGS4 data are plotted in both cases.)

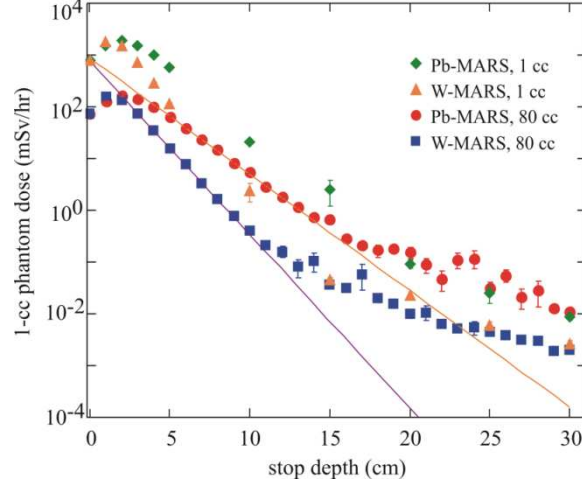


Figure 15: Contact dose-rate calculated with MARS after Pb and W beam stops recorded in both 80 cc and 1 cc phantom volumes. Exponential fits to the 80-cm phantom data in the photon-dominated region are also shown.

the showering GB radiation, only a very small fraction of this radiation spreads outside of the phantom volume. Thus the change in the energy deposited in the phantom versus stop thickness is due almost entirely to attenuation within the stop.

3.3 *y-z Histograms and Abel Inversion*

We have been using Cartesian MARS histograms; however, our geometry possesses some cylindrical symmetry as well. Ignoring the effects of rectangular collimator and shutter apertures and square cross-sectional stops, we expect the 3-D distribution of radiation dose to have cylindrical symmetry about the z -axis at least for radii small compared with the stop dimensions. In this case, we wish to generate an r - z distribution from MARS data to find the maximum dose-rate in a 1-cm^3 cylindrical volume with a scoring area of 1 cm^2 . We further assume the symmetry axis of this volume is aligned with the axis of GB radiation propagation. The 1-cc cylinder will then be a reasonable approximation to the 1-cm cube described above.

An alternative approach to the x - y grid is to use an Abel inversion (AI) of the x - z histogram data presented earlier. An AI could equally be done on an equivalent y - z histogram; an example of y - z dose-rate data equivalent is presented in Fig. 11b. AI provides a useful tool for converting line-averaged Cartesian data into radial profiles. AI is a standard diagnostic technique for extracting electron radial density in plasma columns [38]. The radial dose-rate profile is assumed to be cylindrically symmetric. The radial density (dose) rate can be expressed as,

$$f(r, z) = -\frac{L_y}{\pi} \int_r^a \frac{dF(x, z)}{dx} \frac{dx}{(x^2 - r^2)^{1/2}}, \quad (26)$$

where a is the radial boundary of the dose-rate profile and $F(x, z)$, given in units of mSv/hr , is the y -averaged, x - z dose-rate obtained from MARS across the y -thickness of the phantom, $L_y=20$ cm. The AI technique requires the line density, which is obtained by

taking the product of the average dose-rate, $F(x,z)$, and L_y . Note that because of symmetry, the radial profile can equally be expressed in terms of the x-integrated dose-rates by swapping x and y in Eq.(26).

To evaluate Eq.(26), the derivative with respect to x of $F(x,z)$ at $z=z_{\max}$ is determined by first fitting the average transverse dose-rate profile $F(x,z_{\max})$ with a double Gaussian function of the form,

$$F_f(x, z_{\max}) = A_x(z_{\max}) \exp\left[-\frac{x^2}{x_{e1}(z_{\max})}\right] + B_x(z_{\max}) \exp\left[-\frac{x^2}{x_{e2}(z_{\max})}\right]. \quad (27)$$

The constants to be determined, A_x , x_{e1} , B_x , and x_{e2} will generally be a function of z. The average transverse dose-rate profile usually consists of both narrow and broad distributions; the double Gaussian function allows a more accurate description of the profile over a single Gaussian by fitting both distributions. In Eq.(27), we make the implicit assumption that the peak dose-rate occurs at $x=0$. The derivative of the average dose-rate required in Eq.(26) can now be determined analytically using Eq.(27) as,

$$\frac{dF(x,z)}{dx} \approx \frac{\Delta F_f}{\Delta x} \Big|_{x_i, z=z_{\max}}, \quad (28)$$

where i is the horizontal (x) position index and ΔF_f is the fitted dose increment ($=F_f(x_{i+1}, z_{\max}) - F_f(x_i, z_{\max})$) over the step size, $\Delta x (=0.2 \text{ cm})$, at the longitudinal location of the dose-rate maximum, z_{\max} . The dose-rate radial distribution is obtained with a second fit using Eq.(23), the radial form presented in Section 2 where $D_f(r,z)=f_f(r,z)$. Assuming the minimum volume element to be cylindrical with a cross-sectional area of 1 cm^2 , the dose-rate in 1 cc is obtained by integrating the dose function given in Eq.(23) from $r=0$ to $1/\sqrt{\pi} (=0.564 \text{ cm})$ in two adjacent longitudinal steps ($\Delta z=0.5 \text{ cm}$) including the z-maximum and taking the average,

$$D_{\max} = \frac{1}{2} \left(\frac{2\pi \int_0^{1/\sqrt{\pi}} [rD_f(r, z_{\max,u}) + rD_f(r, z_{\max,d})] dr}{\int_0^{1/\sqrt{\pi}} 2\pi r dr} \right), \quad (29)$$

where the “u” and “d” subscripts on z_{\max} refer to upstream and downstream average dose profiles. Separate fits are performed at both z locations indicated in Eq.(29).

The AI-derived dose-rates are compared with the Cartesian 1-cm cube simulation results in Figure 16. The AI technique appears to reasonably reproduce the results of the 1-cc cube when the stop is thin. For a thin stop, the transverse extent of the radiation is small compared with the stop dimensions. However, a systematic underestimation is

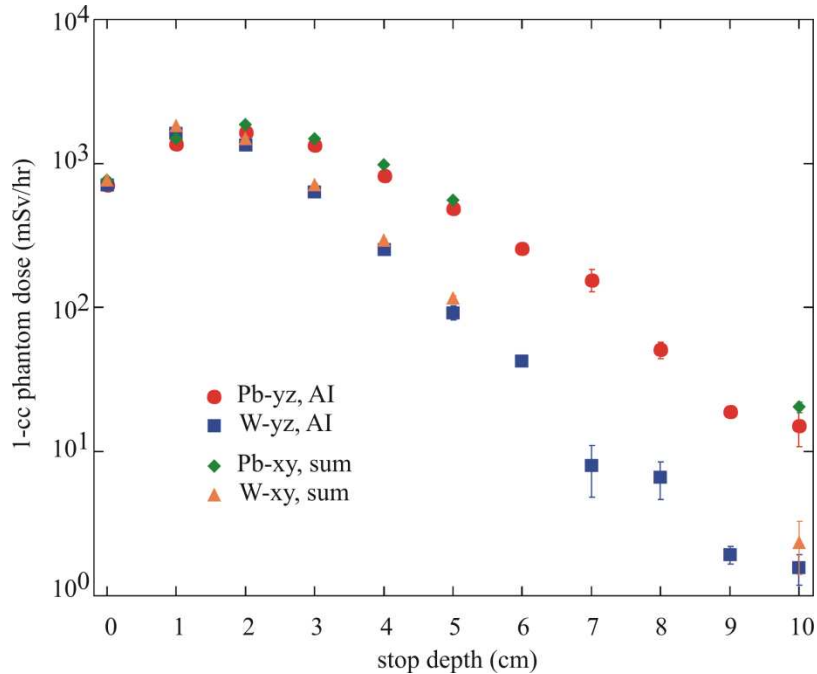


Figure 16: Comparison of 1-cc dose-rate data derived from DET by fitting radial AI profiles (y-z histograms) and summation of x-y histograms.

seen when stop thicknesses exceed 3-4 cm. This probably is due to several effects of which we mention three: First, the fitting process misses more of the radiation distribution for a broader radiation pattern; therefore direct numerical integration should be used. Second, a broad pattern no longer exhibits cylindrical symmetry because the geometry of the stop is square in cross section. Third, the double Gaussian is not a good model for the transverse distribution at least for broader patterns.

3.4 Analysis

Accurate dose estimates require that the radiation be uniform over the volume in which it is being measured; this condition is referred to as having a broad, parallel beam. A related concept is that of charged-particle or electronic equilibrium, which requires that the number of charges entering a volume be equal to the number leaving the same volume [39,40]. Initially, for thin stops, the dose from GB meets neither of these conditions, even for volumes as small as 1 cm^3 . The number of charges leaving a volume exceeds those entering as the shower develops. As the GB radiation is made to travel through greater beam stop thicknesses however, the transverse extent of the radiation pattern grows, and the average energy in the radiation pattern falls below the critical energy. At this point, electronic equilibrium is established. The shower is fully developed and is said to be photon dominated. Charge equilibrium implies that no additional showering will occur, and we are past the point of maximum dose in a phantom.

For both Pb and W, a minimum in the mass attenuation coefficient occurs near 4 MeV, and this becomes the effective energy of the shower until most of these photons

are absorbed. After the photons have been removed, the radiation is composed primarily of photoneutrons, and the spatial pattern becomes very diffuse. As the pattern broadens with increasing stop thickness, dose fluctuations in the 1 cm³ phantom volume begin to grow in the simulation, and the AI method described becomes less accurate. As the GB radiation pattern expands, the 80-cc elements of the segmented phantom shown in Figure 11 may be used to determine the maximum dose. After achievement of both broad-beam and electronic equilibrium, dose results in the two phantom elements are nominally the same. The 1-cc maximum and the central phantom element dose-rates still differ by factors of 2-3 up to stop thicknesses of 10 cm for both Pb and W. For stop thickness of 10 cm, the average FWHM of the radial dose-rate distributions are 4.8 cm and 6.4 cm in Pb and W, respectively. The results indicate that, with respect to the segmented phantom, the condition for a broad beam has still not been obtained for stop thicknesses of 10 cm in either metal, but especially in Pb.

In TB-20, the semi-empirical value given in Table 3 attributed to Franck was used as the reference at zero stop thickness to obtain the dose at a depth of 10 cm. New simulations were then initiated from 10 cm to obtain dose levels at greater depths in the beam stops; this was necessary due to the relatively low number of events tracked (10⁴) in the EGS4 study. Comparing MARS and EGS4 output, the maximum 1-cc dose-rates and attenuation in the photon-dominated regions are approximately the same, as shown Figure 14. For thicker targets however, the dose-rate no longer follows photon attenuation, as PN's begins to dominate. We again note that, at the time the EGS4 simulations were conducted for TB-20, neutron contributions were not included. The authors of TB-20 accounted for the neutrons by assuming they were responsible for half the dose-rate and thereby lowered the dose-rate limits by a factor of 2. The neutron-modified limit is 1.25 μSv/hr. The reference dose-rate level was used as a limiting value in TB-20 for determining beam stop thicknesses. The reduction in the reference level does not apply to MARS, which includes neutron production; therefore, the dose limit for MARS data should be set at 2.5 μSv/hr for comparative purposes.

The EGS4 results from TB-20 are fit with exponentials in Fig. 14 as are MARS data in the photon-dominated regions shown in Fig. 15. The coefficient of the exponent should approximately represent the minimum mass attenuation coefficient for each metal. The mass attenuation coefficients for Pb and W are given in Table 5. These coefficients

Table 5. Mass attenuation coefficients for Pb and W comparing EGS4 and MARS with minimum attenuation near 4 MeV.

	μ/ρ (4 MeV) (cm ² /g)	μ/ρ EGS4 (cm ² /g)	μ/ρ MARS (cm ² /g)
Pb	0.0420	0.0439±.0089	0.0456±.0033
W	0.0404	0.0341±.0051	0.0401±.0019

are compared with minimum mass attenuation values given by Hubbell [41,42]. The EGS4 results indicate the attenuation in Pb and W is 4 percent higher and 16 percent lower than the Hubbell values, respectively. The fluctuations in the EGS4 results may be due more to the small data sample than any real variation. MARS mass attenuation coefficients are 9 percent higher and 1 percent lower than the respective minimums. One

might expect the attenuation coefficients from simulations to be slightly higher than the minimum values owing to finite energy spread of the shower. The simulated shower will always have particles away from the minimum attenuation energy.

The breakpoints in thick targets where contributions from PNs dominate the total dose-rate occur near 15 cm in Pb and 10 cm in W. For a target thickness of 25 cm or greater, the number of events per MARS run is increased from 10^8 to 2×10^8 . Statistics on the total dose are obtained by running 10 cases for each material and thickness, varying the initial seed for each case. Also, extrapolating back to zero thickness, one sees a clear indication of the build-up of dose-rate as the shower progresses through the stop.

4. Photoneutron (PN) Production

4.1 Description

A study of PN dose resulting from GB [9,21] striking thick targets of differing metals was conducted by Pisharody et al. [5,6]; specifically, the metals examined were Fe, Cu, W, and Pb. A comparison of these data with MARS simulations is presented here to evaluate its predictive capability for simulating PN dose. In References 5 and 6, an Andersson-Braun (AB) remmeter was used to measure the PN dose. The plan geometry of the MARS simulation is presented in Figure 17; in this case, an iron target receives the GB beam. The simulation dose is again recorded in a tissue phantom, 20 cm by 20 cm in transverse dimensions (y and z) and 30 cm in depth (x), relative to the incident beam. In Fig. 17b, a contour plot of the PN dose predicted by MARS is shown for the geometry given in Fig. 17a. The simulation results presented in Fig. 17b must be normalized for the actual pressure and current as mentioned above. Performing this normalization, PN dose results from measurements given in Ref. 5 and 6 and scaled MARS simulation output are presented for comparison in Tables 6 and 7. The simulations start with 2×10^8 primary electrons striking the air target 31 m upstream of the GB beam stop. Ten independent cases (separate seeds) are then averaged to produce the neutron dose

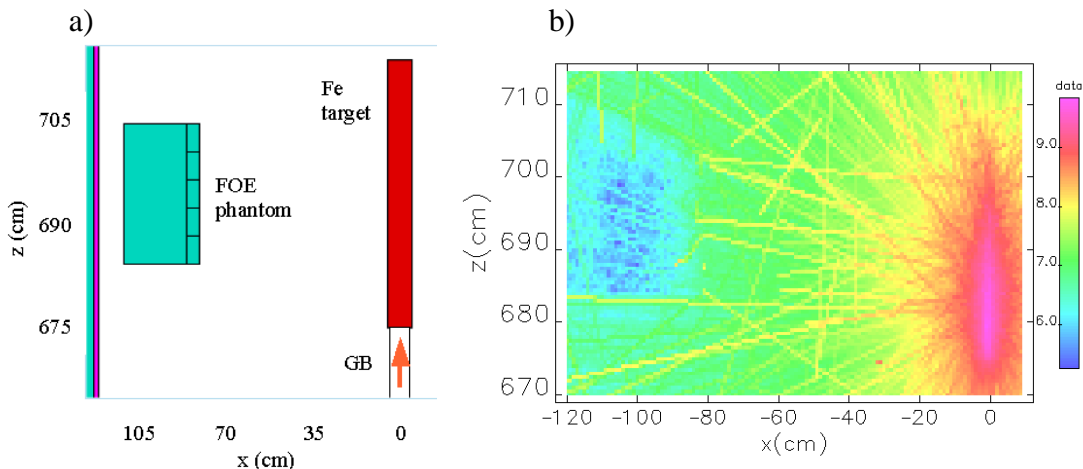


Figure 17: a) Plan geometry of the MARS PN measurement simulation and b) contour plot of uncorrected MARS PN dose-rate ($\log_{10}[\text{DEN}(\text{mSv/hr})]$) from GB beam striking the cylindrical Fe target shown in a) without a mask. The thickness in the y-direction is 20 cm centered at beam elevation.

recorded in the FOE phantom. Note that the phantom is segmented as described earlier. The 5x5, 80-cc tissue array closest to the target provides the “shallow” dose equivalent listed in the tables; the full dose equivalent is derived from the entire phantom.

In addition to physical parameters that affect GB, such as background gas pressure and composition, the geometry of the beamline must be properly considered. Inclusion of the front end (FE) exit mask(s) is necessary to accurately assess the PN dose in the FOE. Though located in the FOE, the exit mask is considered the last element in the FE beamline. The exit mask used at the time the PN measurements were made [5,6] is shown in Figure 18a. The cut-away elevation view shows the copper tapering at a 2°

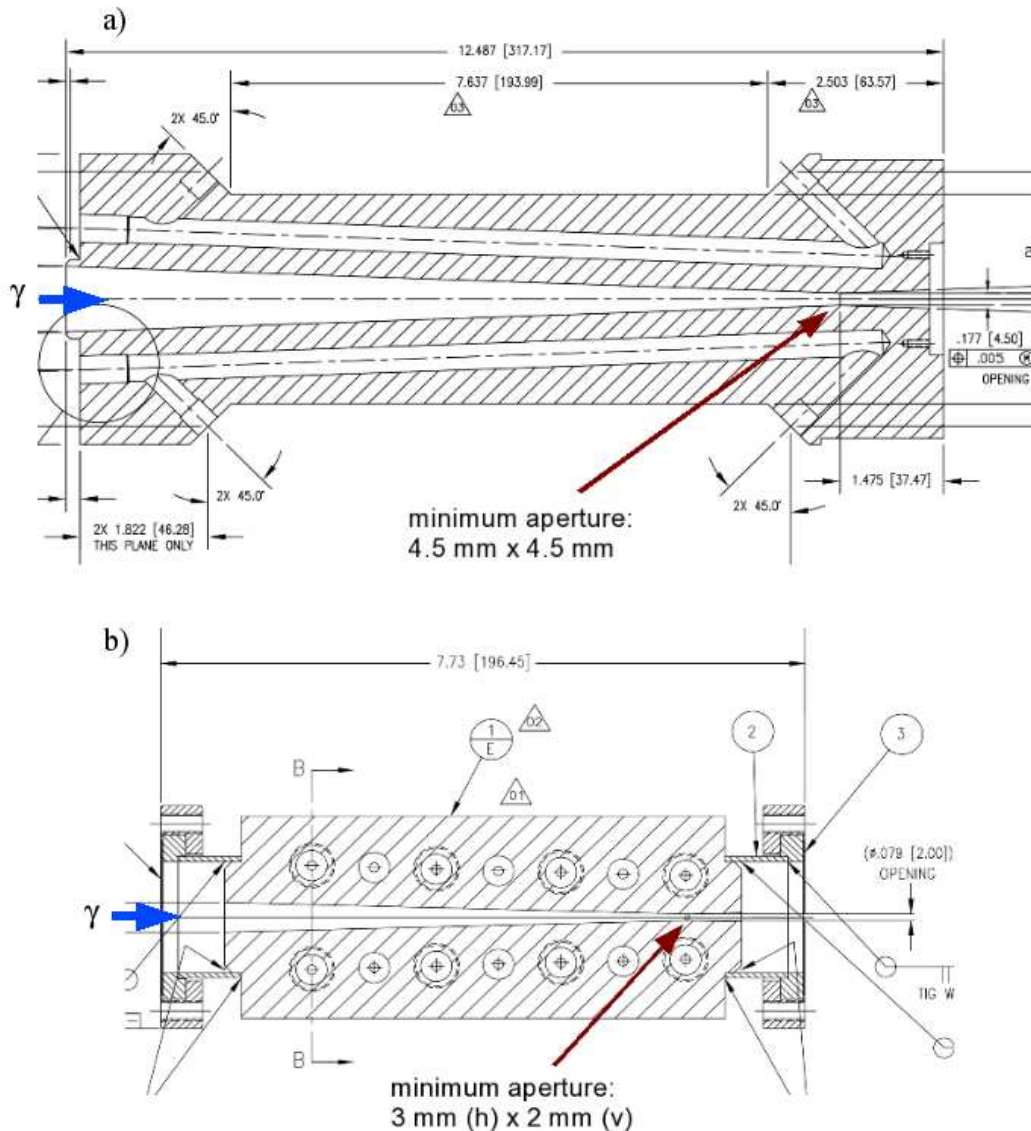


Figure 18: Cut-away elevation views of copper masks used at the terminus of the beamline front end (FE) within the first optics enclosure (FOE); a) original 4.5 x 4.5 mm² mask and b) present 3 x 2 mm² fixed exit mask. The GB and x-ray photons enter from the left. In some beamlines, both masks are used.

angle to a minimum y-aperture of 4.5 mm. In the x-direction, the aperture is also tapering to a minimum width of 4.5 mm, though with a taper angle of 4°. Based on the transverse distribution shown in Section 2, it is clear that the edge of the GB radiation will be intercepted by the mask. At $r=2.25$ mm, the GB density is approximately 37% of the peak value. At its minimum, the aperture is roughly square, whereas the beam is round; also, the mask tapers more rapidly in x than in y. One should therefore expect that cylindrical symmetry in the radiation pattern immediately downstream of the mask will be lost. As the aperture of the mask shrinks with z, so does the thickness of copper in the z-direction. A significant amount of scattered radiation (“secondary bremsstrahlung”) results from the primary GB photons striking the mask. The effect of masks on the radiation profiles around the FOE will be discussed in greater detail in Section 5. Recently, the smaller aperture exit mask shown in Fig. 18b is being utilized in beamlines, particularly in those with canted undulators [43]. In this case, the x and y apertures are 3 mm and 2 mm. For $r=1$ mm, the GB distribution according to Eq.(23) is 78% of the peak value. At 1 mm the vertical edge mask is well into the GB radiation.

4.2 Previous PN Dose Measurements and Comparisons with MARS.

The PN measurements presented in Table 6 are obtained from beamline 6-ID, which has the lowest GB power of all beamlines examined; a factor of 3 below the average [23]. Table 7 presents a comparison of MARS with measurements made for beamline 11-ID.

Table 6: Comparison of PN dose-rate measurements made in Refs. 5 and 6 for beamline 6-ID with MARS simulations correcting for differences in Z_{eff} between air (7.3) used in MARS and a measured value of 4.08. Dose recorded in shallow (sh) and full phantom regions are given; the last three rows are MARS simulations denoted with mask configurations.

Target Material	Fe		Cu		W		Pb	
I (mA)	93.1		90.1		88.5		76.1	
P (nT)	9.69		9.41		9.29		8.22	
AB Remmeter ($\mu\text{Sv/hr}$)	0.150		0.130		0.186		0.177	
phant. region	sh	full	sh	full	sh	full	sh	full
MARS, no mask ($\mu\text{Sv/hr}$)	1.007	0.321	1.403	0.561	1.129	0.422	1.001	0.268
4.5 x 4.5 mm ²	0.659	0.289	0.629	0.229	0.616	0.201	0.786	0.228
3 x 2 mm ²	0.337	0.135	0.362	0.199	0.265	0.090	0.288	0.096

In Table 6, the measured PN dose-rate for Fe is the average for the two highest current levels (93.4 and 92.7 mA) in Table 6 of Refs. 5 and 6, likewise for Cu and W, and from the highest current for Pb. In Table 7, the measured PN dose-rate for Fe is the average of the three highest current levels (96.6, 93.3, and 90.2 mA) in Table 5 of Refs. 5

Table 7: Comparison of PN dose-rate measurements made in Refs. 5 and 6 for beamline 11-ID with MARS simulations correcting for differences in Z_{eff} between air (7.3) used in MARS and a measured value of 3.18. Again, dose-rate recorded in shallow and full phantom regions are given; the last three rows are MARS simulations denoted with mask configurations.

Target Material	Fe		Cu		W		Pb	
I (mA)	93.4		92.2		78.4		76.2	
P (nT)	8.97		8.88		7.78		7.54	
AB Remmeter ($\mu\text{Sv/hr}$)	0.371		0.462		0.393		0.425	
phant. region	sh	full	sh	full	sh	full	sh	full
MARS, no mask ($\mu\text{Sv/hr}$)	0.600	0.191	0.869	0.347	0.537	0.201	0.590	0.158
4.5 x 4.5 mm ²	0.392	0.172	0.390	0.142	0.293	0.095	0.463	0.134
3 x 2 mm ²	0.201	0.080	0.224	0.124	0.126	0.043	0.170	0.057

and 6, likewise for Cu, but the lowest three for W and Pb. Actual target dimensions in the experiment were varied to maintain lengths of $20X_0$ and diameters of $6R_M$, where X_0 is the radiation length and R_M is the Moliere radius.

In the Tables 6 and 7, simulated dose recorded in shallow (“sh”) and full phantom regions are used for comparison with measurements. Whereas in Section 2 only the central 80 cc volume of the segmented phantom region was used for dose calculations; here, the entire segmented region (20 cm x 20 cm x 5 cm) comprises the volume for the “shallow” entry. Note that use of the term “shallow” here should not connote a formal definition. According to 10CFR835 [44], “For external dose, the equivalent dose to the whole body is assessed at a depth of 1 cm in tissue;...” therefore the “sh” entries might more appropriately be considered “whole body” or deep dose equivalent results.

4.3 Comments on PN Dose Measurements and Simulations

The simulated dose-rates given in Table 6 for beamline 6-ID are approximately 3-5 times larger than the measured values; whereas those given in Table 7 for beamline 11-ID are much closer. Several reasons exist that may explain the differences in the two sets of results:

- 1) Residual gas Z_{eff} . The target used in MARS to generate the gas bremsstrahlung beam is composed of air with a $Z_{\text{eff}}=7.3$; however, the Z_{eff} for 6-ID (measured close to the center of the ID straight section) is given as 4.08. The ratio of GB power in air to that for 6-ID given this difference in Z_{eff} is 2.8. The difference in Z_{eff} is accounted for in both Tables 6 and 7; however, even with these measurements, the actual Z_{eff} in the undulator beamlines are difficult to definitively ascertain. In the case of Table 6, to reduce the MARS results by an additional factor of 4 would require $Z_{\text{eff}}\approx 2.2$; based on other RGA measurements, this value of Z_{eff} is probably unlikely.

- 2) Residual gas pressure. Another parameter that can vary from beamline to beamline is the background gas pressure. The Z_{eff} quoted for 11-ID is 3.18, yet the GB power from this line is 3-4 times higher than that of 6-ID. This suggests that the pressure or other factors (see item 3) may be considerably different for these two lines.
- 3) Beam pipe misalignment. Prior to the installation of an ID in the 6-ID undulator straight section, but after the GB measurements had been made, a 1-mrad bend in the beam central orbit trajectory was noted through this region. The misalignment may have reduced the GB power by a factor of 3 in 6-ID. Though a factor of 3 does not explain the full difference between measured and simulated value, it brings the level of agreement with all values to between 60 and 90 percent.
- 4) Collimation by masks. The inclusion of the proper FE exit mask or masks is necessary to obtain useful PN results.
- 5) Detector energy dependence. A correction was made to the original PN data taken with an Andersson-Braun (AB) remmeter; additional corrections are possible but likely to be small.
- 6) Correct interpretation of the segmented phantom dose used in the simulation. The upstream region (closest to the GB target) is equivalent to the deep dose value reported by the AB remmeter.

In conclusion, a number of factors can influence the PN dose-rate. Given the uncertainty in local values of pressure and Z , the degree of agreement between MARS and the PN measurements is good when using the $4.5 \times 4.5 \text{ mm}^2$ mask “shallow” results. Again measuring the GB power in some of these lines while varying local pressure would be useful; alternatively, having a good model of the ID straight section pressure profile [25], as mentioned earlier in Section 2, would also be desirable. The PN production in MARS is benchmarked in Appendix A against calculations made with FLUKA.

5. First Optics Enclosure (FOE) Studies

In the previous section, we saw it was important to use actual pressure and gas composition (Z_{eff}) to obtain accurate PN dose values. The same will be true as dose levels in the FOE are assessed. At 300 mA, extrapolating the pressure versus current data given in Ref. 6 with linear fits predicts an average background gas pressure of 27 nTorr. For Z_{eff} , the average of values from Refs. 6 and 23 are used, thus $Z_{\text{eff}}=4.0$.

Two simulation studies have been conducted with MARS to assess shielding requirements. In the first study, dose-rate levels in contact with the outside-wall of the FOE are examined when GB radiation strikes Pb or W beam stops within the FOE. The overall FOE geometry is similar to that presented in Figure 5 of TB-7. In the MARS FOE geometry, $z=0$ corresponds to the upstream edge of the FOE inner wall. The upstream edge of the beam stop is positioned at $z=675 \text{ cm}$. Figure 19 shows a transverse,

elevation view of the MARS FOE geometry at $z=675$ cm. The beam is offset by -15 cm in the y direction to minimize the volume used in the MARS simulations. A plan view of the MARS geometry used to model the FOE is shown in Figure 20a. The Pb-brick, ratchet wall collimator is located at the upstream end of the FOE. Aperture dimensions through the collimator are 5.588 cm horizontally and 2.54 cm vertically. Upstream of the ratchet wall collimator are the two tungsten safety shutters each 30 cm in length apertures of 7.2 cm in x and 2.0 cm in y . A copper exit mask is seen downstream of the wall collimator.

We focus our interest on the dose-rate in two planes: 1) horizontal at beam elevation ($y=-15$ cm) along the outside-wall of the FOE and along the FOE back wall, and 2) vertical along the beam axis ($x=0$) on the FOE roof and back wall. The transverse dimensions of the stop are varied to obtain dose sensitivity outside the enclosure. The FOE Pb shielding thicknesses used are 19 mm for the outside wall, 50 mm plus an additional 50 mm by 1-m^2 sheet centered on the beamline for the back wall, and 12 mm for the roof.

In the second study, the thickness of lead required to shield against the GB extremal ray is determined. The initial approach with MARS was to repeat the geometry described

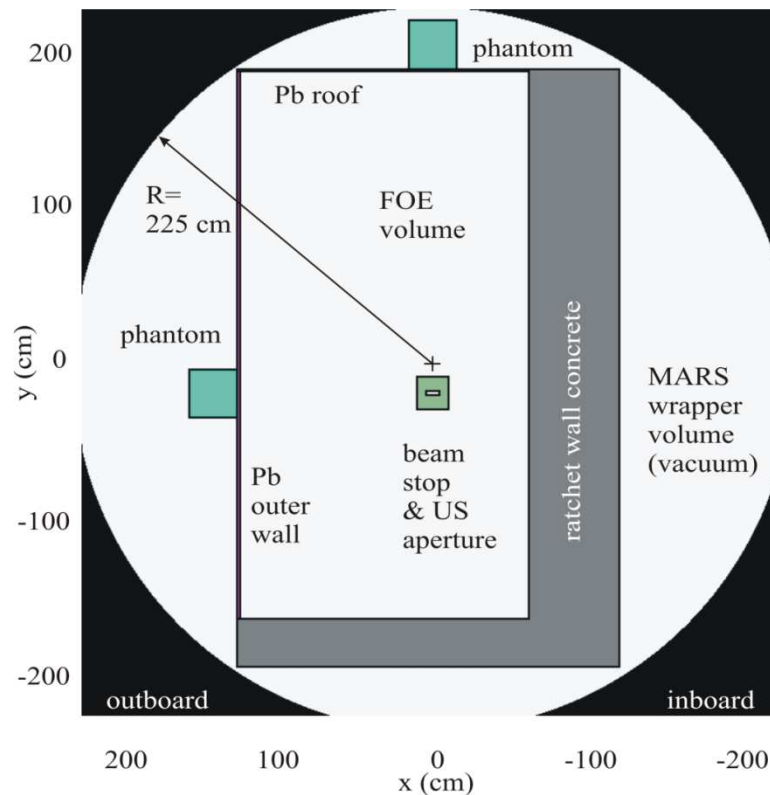


Figure 19: Transverse FOE geometry used in MARS at $z=675$ cm, the upstream edge of the beam stop. Note that the geometry is offset in y with respect to beam elevation to minimize the wrapper volume; beam elevation is positioned at $y=-15$ cm.

in TB-20; however, this method proved unsatisfactory when modeled with MARS and was abandoned in favor of an alternate approach. A discussion of the TB-20 extremal ray methodology is provided in Appendix B along with modeling results from MARS.

In both studies, 500 mrem/year (5.0 mSv per year) or 250 μ rem/hr (2.5 μ Sv/hr) for 2000 hours is used as the limiting dose-rate to compare with earlier calculations in TB-7 and TB-20. As mentioned earlier, in TB-20, half of the dose-rate is ascribed to neutrons, which were not simulated; therefore, the dose-rate limit used in that study was 1.25 μ Sv/hr. MARS simulations include photoneutrons in the dose calculations; therefore, the dose level is restored to 2.5 μ Sv/hr. Prior to presenting the results from the two aforementioned studies, it is first important to describe how dose-rate is measured using MARS. MARS provides two approaches for obtaining dose: 1) histograms specified in the “XYZHIS.INP” file and 2) element geometry entered in the “GEOM.INP” file; these methods are described in the following section.

5.1 MARS Dose Determination

MARS provides several dose equivalent output histograms. For example, one dose-equivalent histogram for neutrons (DEN) was shown in Figure 17 of the previous section. In the present section, the total dose-equivalent histogram (DET) is employed; DET sums the dose from all radiation components, including photons, electrons, and neutrons. A histogram is defined in three Cartesian dimensions (hence the name of the input file, XYZHIS.INP) by giving a range for each dimension (three pairs of numbers with minimums given first and maximums second), as well as the number of times each dimension is to be divided. For example, in the FOE, dose in the x-direction of the horizontal plane is specified with a width, $L_x=300$ cm, centered on the beam axis ($x=0$) and divided into 150 equal segments ($\Delta x=2$ cm). In the longitudinal direction, the histogram length, $L_z=1000$ cm and is divided into 200 equal segments ($\Delta z=5$ cm). In the z-direction, the histogram is positioned to include the upstream ratchet wall, as well as the region just downstream of the back wall as shown in Figure 20a. The height of the histogram is 24 cm, centered on beam elevation ($y=-25$ cm) and is undivided. The two input lines in the XYZHIS.INP file that specify this geometry, as well as which histograms to generate, are as follows:

```
xyz  -150.  150.  -27.0  -3.0  -180.  820.  150  1 200  XZ_air_shower
FLE FLM FLN FLG DEN DEG DET
```

The histogram in the vertical plane containing the beam axis is similarly specified:

```
xyz  -12.  12.  -180.  210.  -180.  820.  1 195 200  YZ_air_shower
FLE FLM FLN FLG DEN DEG DET
```

Note that in the vertical plane, the x-dimension is undivided. Again, the histogram input file does not specify the actual geometry of the simulation, and it is up to the user to place the histograms properly. Examples of XYZHIS.INP, GEOM.INP, and MARS.INP files used in this study can be found in Appendix C.

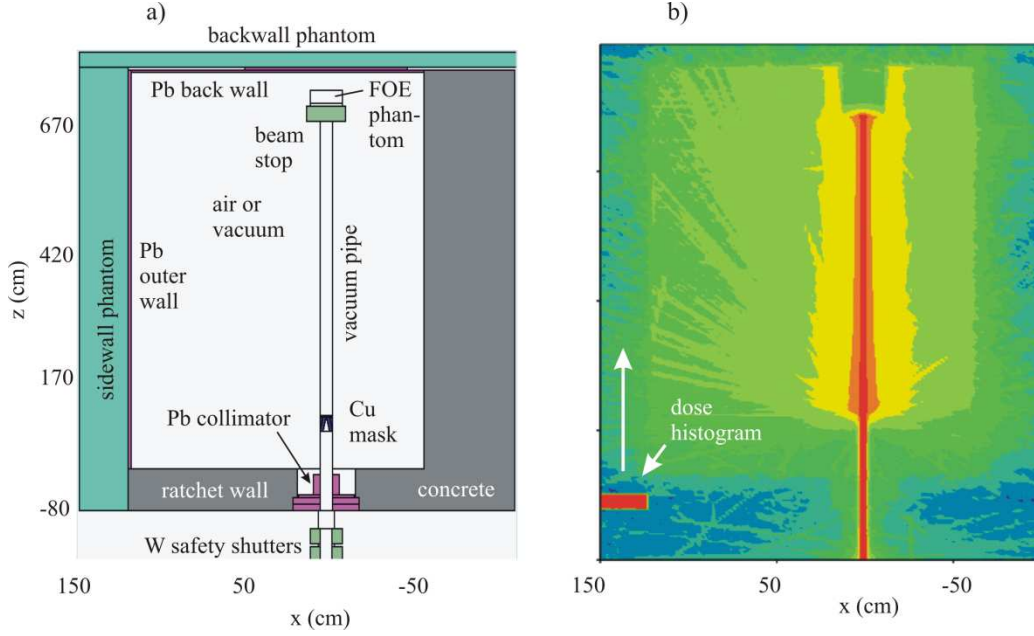


Figure 20: a) MARS FOE geometry in the x - z plane at beam elevation and b) DET histogram of the same region. The DET z -profiles are obtained by translating the dose histogram along z , outside of the FOE wall. The z -scale is compressed by a factor of 3.1 relative to x .

Each volume element specified in a histogram is referred to as a voxel. In the case of the DET histograms, each voxel records the dose-rate in a tissue region defined in the geometry input file, "GEOM.INP." In this report, dose-rate histograms (DHs) are used to determine the dose-rates in regions occupied by tissue-equivalent phantoms. The DHs should not be used in regions of low density or vacuum without a tissue phantom present. The DH is a collection of adjacent voxels of a size determined in XYZHIS.INP file in which the dose is collected. The location is then varied in a defined manner to create a dose profile. For example, the dose profile specified along the outer wall of the FOE (z -direction) is defined as,

$$\dot{D}(z_u) = \frac{1}{N_t} \left(\sum_s^{N_{pz}} \sum_r^{N_{px}} \text{DET}_{r+N_{x0}, s+N_{z0}+uN_{pz}} \right), \quad (30)$$

where DET is the 2-D histogram matrix, N_{pz} and N_{px} are the number of voxels within the DH in the z - and x -directions, $N_t = N_{px}N_{pz}$ is the total number of voxel in the DH, N_{x0} and N_{z0} are the starting position indices in x and z , and u is the index of the DH z coordinate where,

$$z_u = \left(uN_{pz} + N_{z0} \right) \Delta z + z_0 + \frac{L_z}{2}, \quad (31)$$

and L_z is the length of the DH, and z_0 is the minimum edge of the geometry both in the z -direction. For the x - z DET histogram presented in Figure 20b, $L_z=30$ cm ($N_{pz}=6$), $L_x=28$

cm ($N_{px}=14$), $z_0=-180$ cm, $N_{x0}=0$, and $N_{z0}=20$. The number of full steps in the DH z-profile is determined from,

$$N_{zdh} = \left(\frac{L_{tz}}{L_z} - \frac{N_{z0}}{N_{pz}} \right) - \text{mod} \left(\frac{L_{tz}}{L_z} - \frac{N_{z0}}{N_{pz}}, 1 \right), \quad (32)$$

$$= 30$$

where the modulus function is used; again, L_{tz} is the total length of the simulation region in the axial (beam) direction. In the example above, dose is determined from the average of 84 voxels per DH step. A similar methodology is employed in the other transverse dimensions. The individual histograms themselves are written as binary objects within the “mars.hbook” output file. The CERNLIB program paw++ has been used to extract the histogram data files into ASCII text files. Recently, effort has been made to speed the extraction process using Self-Describing Data Set (SDDS) tools available at the APS [45]. In particular, the GB DET histograms in Fig. 13 and the PN DEN histogram in Figure 17 have been extracted and plotted using these tools [46].

As mentioned above, summing dose equivalent output (for example, DEN, DEG, or DET) in a DH region should only be done in volumes specified with tissue phantoms; otherwise the DH will yield erroneous dose results.

MARS provides an alternative method to obtain dose in the form of MTUPLE output files (“MTUPLE.EXG” for extended geometry cases of the type used here); EGS4 employs a similar approach. The MARS MTUPLE file provides various doses in geometrical elements specified in the input geometry file. The MTUPLE dose categories include the total dose equivalent (DEQ) analogous to DET histogram data. Note that both histogram and MTUPLE MARS output provide dose-equivalent results specified in units of mSv; thus quality factors are already included in the output data sets. Normalizations of the dose-equivalent output differ for the two cases, however. For histogram output, DET units are specified as mSv per total charge (e.g., 300 mA= 1.873×10^{18} e/s); whereas, in MTUPLE output, DEQ is given in units of mSv per primary particle (ppp).

Four right-rectangular phantom regions are used in the FOE study: 1) in contact with the outside wall at beam elevation, 2) in contact with the roof centered at the horizontal beam position, 3) horizontally along the back wall at beam elevation, and 4) vertically along the back wall again centered horizontally at the beam position. For all simulation data presented below in Figures 21-28, the electron beam current is 300 mA and beam energy is 7 GeV. Masks are included in all simulation results except Fig. 28, where a well-defined GB beam is desired. The straight section background gas pressure is assumed to be 27 nTorr with a Z_{eff} of 4.0; the exception again is Fig. 28, where a pressure of 1 nTorr and a Z_{eff} of 7.3 (air) are used.

5.2 Effects of Masks in the FOE

The exit masks have a strong effect on radiation in the FOE. Collimators are typically used downstream of the FE exit mask to stop the secondary bremsstrahlung; however, because these collimators are reconfigurable, we do not consider them in the simulations. An example of the dose profiles in the outside wall phantom region (at

beam elevation) is presented in Figure 21 for the case of no mask, a 4.5 mm square mask, only, and both the 4.5 mm and the 3 mm x 2 mm masks. A similar pattern, though a lower dose level is observed along the phantom on the roof of the FOE as shown in Figure 22. The masks cause a significant modification to the dose profile along the z-direction shifting the peak upstream closer to the scattering source.

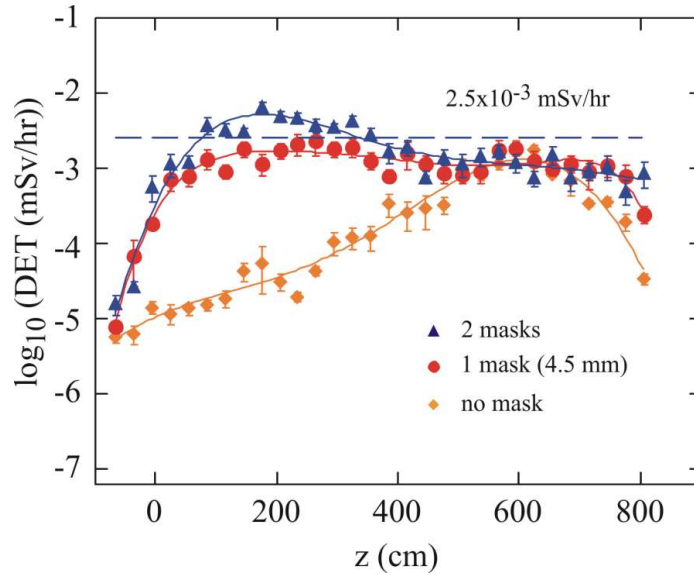


Figure 21: Dose-rate profiles in the outside wall phantom with differing masks. The radial profile of the GB radiation is shown in Section 2, Fig. 9. The reference dose-rate level of $2.5 \mu\text{Sv/hr}$ is indicated. The beam stop is 20-cm-square cross section by 30-cm-length tungsten.

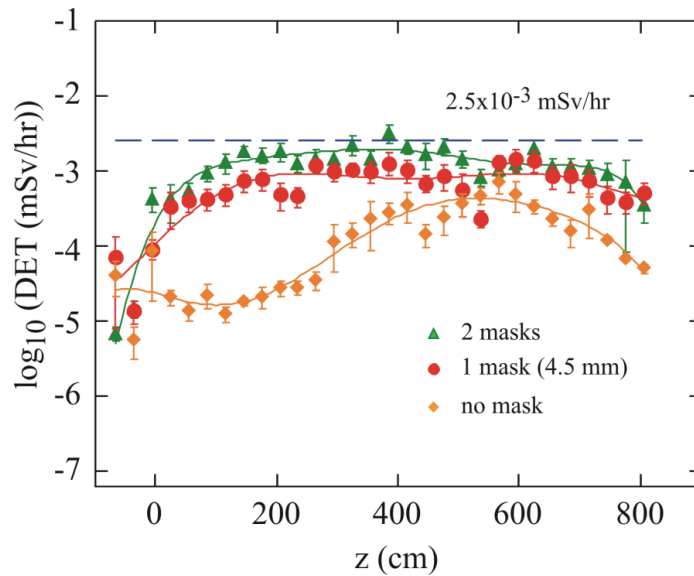


Figure 22: Dose-rate profiles in the roof phantom with differing masks. The reference dose-rate level of $2.5 \mu\text{Sv/hr}$ is indicated. The beam stop is 20-cm-square cross section by 30-cm-length tungsten.

Dose-rate patterns along the back wall are also substantially modified relative to the case with no mask. The back wall phantom profiles in both the horizontal and vertical planes are shown in Figures 23 and 24. Without further collimation, the dose-rates push significantly above the $2.5 \mu\text{Sv/hr}$ level at 300 mA. Note that at 200 mA, nominal dose-rates should be reduced by a factor of $1.5^2=2.25$.

5.3 FOE Beam Stop Transverse Dimensions and Material

We next examine the dose-rate while varying the beam stop transverse size. The stop is assumed to be a right-rectangular prism 30 cm in length. The cross section of the stop perpendicular to the GB beam is square, and therefore the transverse dimensions are characterized by a single value. The full transverse size of the Pb beam stop is varied from 12 to 24 cm. Dose equivalent profiles are obtained by translating the red DH region shown in Fig. 20a in a step-wise fashion along the axis of interest as described above. In all cases, the material assigned to the geometry representing the FOE phantom shown in Fig. 20a is set to vacuum. The log of the dose-rate data are fit with sixth-order polynomials using a least-squares algorithm found in the mathematical application software, MathCAD [47]. The polynomial fits help to smooth the statistical nature of the low-level dose.

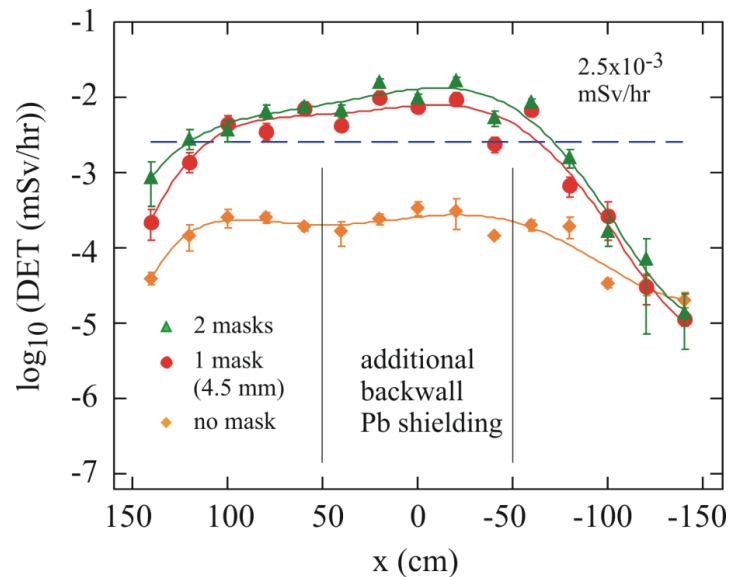


Figure 23: Back wall dose-rate in the horizontal plane for 0, 1, and 2 masks. The beam stop is 20-cm-square cross section by 30-cm-length tungsten.

Variations in beam stop dimension (a square cross section is being assumed) along the side and back walls are given in Figures 25 and 26. Little difference is observed in the profiles along the side wall for stop sizes of 12 and 24 cm in W, except in the region of the stop itself. Finally a comparison of beam stop materials (Pb or W) is presented in Figure 27 along the horizontal back wall. For both stops a transverse size of 24 cm is chosen.

The statistics present in the DH data shown in the DET profiles plotted in Figs. 21-27 are based on ten MARS runs. Each run starts with a different random seed.

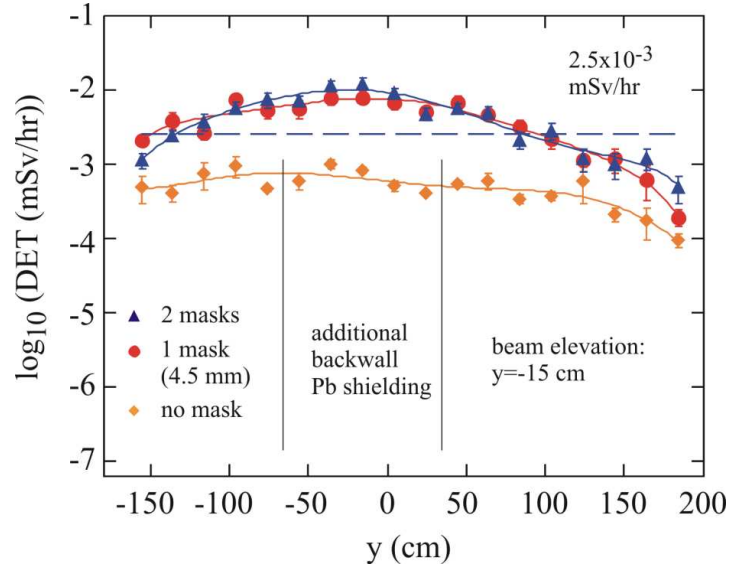


Figure 24: Back wall dose-rate in the vertical plane for 0, 1, and 2 masks. Note the offset in beam elevation. Beam height is set at $y = -15 \text{ cm}$, as indicated Fig. 19. The beam stop is 20-cm-square cross section by 30-cm-length tungsten.

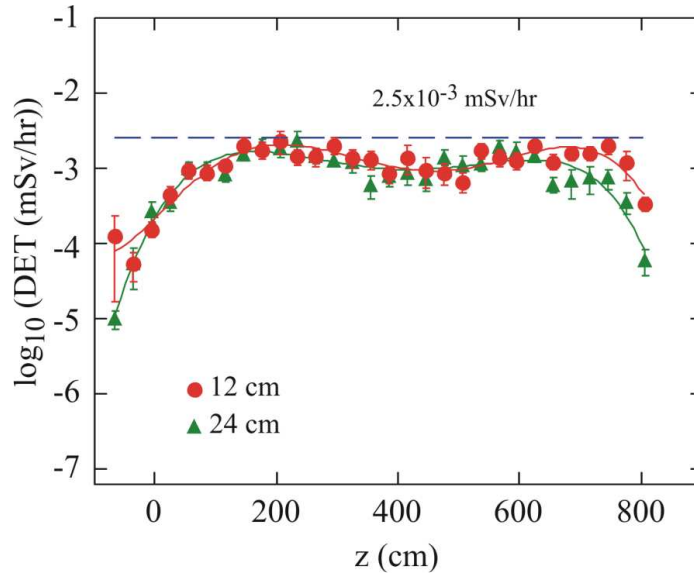


Figure 25: Side wall phantom dose-rate for W beam stop transverse dimensions of 12 and 24 cm. The most significant difference occurs in the region of the stop. A single $4.5 \times 4.5 \text{ mm}^2$ mask is included in the simulation.

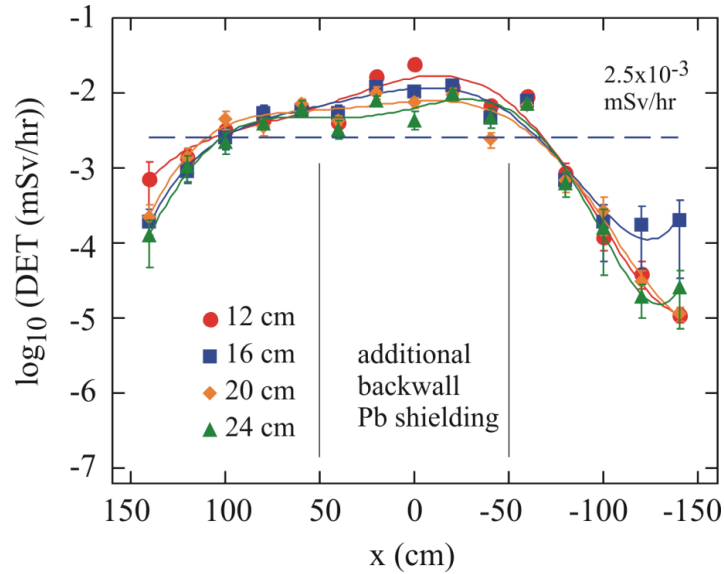


Figure 26: Back wall dose-rate profiles in the horizontal plane for W beam stops of differing transverse dimensions. A single $4.5 \times 4.5 \text{ mm}^2$ mask is included in the simulation.

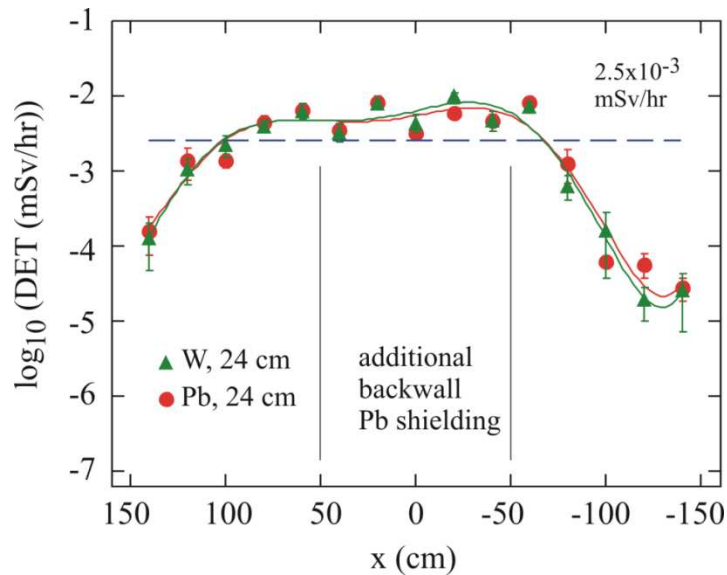


Figure 27: Comparison of horizontal back wall dose-rate for Pb and W 24-cm-square beam stops. A single $4.5 \times 4.5 \text{ mm}^2$ mask is included in the simulation.

5.4 Extremal Ray

Dose-rate from GB radiation striking a thick target scatterer within a beam pipe is simulated to compare with a similar analysis given in TB-20 to determine the extremal ray requirement. After using MARS to review the earlier approach (see Appendix B), the determination was made to investigate an alternative method. The geometry used for the

new study described here is simple and obtained by replacing the square cross-section beam stop with a cylinder of the same length, 30 cm. The radius of a Pb target is varied, while dose is recorded using the back wall tissue phantom.

Determination of the extremal ray distance requires knowledge of the GB beam size, which is provided in Section 2. For the smallest target radii, a fraction of the primary GB beam passes by the target altogether (or perhaps experiences one scattering within the Moliere radius) and directly strikes the Pb shielding on the back wall. A fraction of this radiation then showers through the shielding to the back wall phantom. Dose-rate in the back wall phantom as a function of target radii is shown in Figure 28. The dose-rate is determined from phantom geometry DEQ values given in the MARS extended geometry output file MTUPLE.EXG as discussed earlier. For radii of 3 cm and above, primary bremsstrahlung is essentially blocked. Dose-rate in the phantom varies weakly with target radius for $r > 3$ cm. The simulations carried out for the data presented in Figure 28 are done at 1 nTorr of background gas pressure; absolute dose values are not important in this case.

The dose in the phantom appears to be characterized by two behaviors: 1) a large variation with radius for small target dimensions and 2) a much smaller change for larger radii. The small radius dose appears to be the result of direct primary GB on the FOE back wall, as well as scattering up to the Moliere radius. The Moliere radius, the characteristic transverse dimension of the shower, may be written as [17],

$$R_m = X_o \frac{E_s}{E_c}, \quad (33)$$

where $E_s = \sqrt{(4\pi/\alpha)m_e c^2} = 21.2$ MeV and the critical energy may be expressed as,

$$E_c(\text{MeV}) = \frac{800}{Z+1.2}. \quad (34)$$

The critical energy in Pb is 9.6 MeV, the radiation length is 5.8 g/cm², and the Moliere radius is 12.8 g/cm². In terms of physical length, the Moliere radius = $R_m/\rho_{\text{Pb}} = 1.1$ cm. Assuming the beam edge radius, r_e , to be twice the FWHM value given in Fig. 9, then $r_e = 2(0.356 \text{ cm}) = 0.712$ cm. The extremal distance, r_{ed} is taken to be the difference between the back wall phantom dose breakpoint radius, r_{bp} and the beam edge radius, $r_{\text{ed}} = r_{\text{bp}} - r_e$. As shown in Fig. 28, $r_{\text{bp}} = 2.7$ cm; thus, $r_{\text{ed}} = 1.988 \text{ cm} \approx 2.0$ cm. Relative to the Moliere radius, the separation thickness is $2.0 \text{ cm}/1.1 \text{ cm} = 1.82 \approx 2$; therefore, the separation between the extremal ray and the edge of the shielding is $2R_m$. In the context of TB-20 therefore, an extremal ray should come no closer than 2.2 cm to the lateral edge in Pb. For W with a Moliere radius of 0.65 cm, a similar argument sets the extremal ray shield edge separation at 1.3 cm. TB-20 [2] recommended that the extremal ray in the case of bremsstrahlung ray-tracing should not be closer than 4.5 cm from the lateral beam stop edge in Pb and 3.0 cm in W; this represented a range between $4.1R_m$ and $4.6R_m$ in the respective metals.

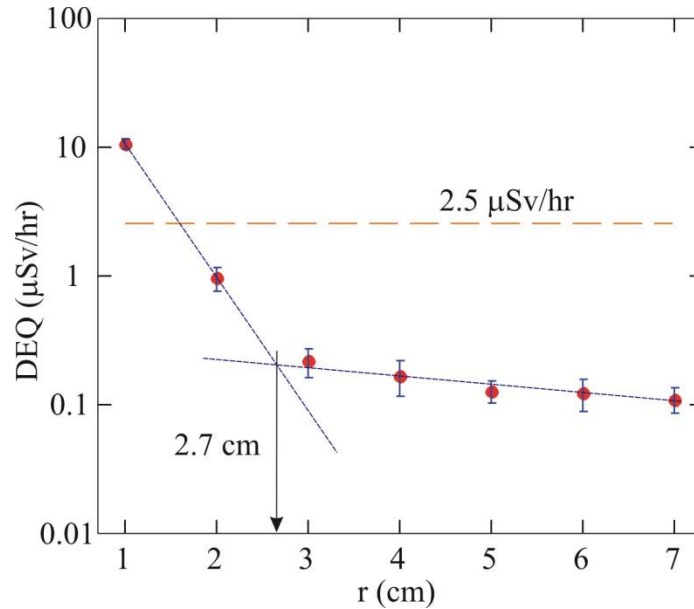


Figure 28: Back wall phantom dose-rate versus beam target radius. The intersection of the fast and slow response curves represents the minimum radius of the Pb stop required to fully shield the back wall phantom from direct GB radiation. The maximum extent of the GB beam is $2 \times \text{FWHM} = 0.71$ cm.

6. Discussion and Summary

6.1 Dose Results

The GB power predicted by MARS gamma fluence spectrum agrees very well with the analytical model, see Table 2. The slight enhancement of the low-energy MARS spectrum does not appreciably affect the integrated result. Given the two independent methods employed, one should conclude that MARS does reasonably well simulating GB power. Analysis and simulation both are in reasonable agreement with the measured GB power associated with PN measurements. Possible explanations for discrepancies were presented in Section 4 and include uncertainty in beamline Z_{eff} , pressure, and undulator straight section alignment. MARS provides a reasonably accurate representation of the GB spatial distribution, in agreement with thin-target GB theory; however, as shown in Fig. 10, care must be taken not to make the air target too thick. An air target pressure of 1 atmosphere and length of 24 cm appears to be a good upper limit.

Initial maximum dose-rates predicted by MARS and the analytical model show good agreement between them; in addition, reasonably similar results are obtained with EGS4 in TB-20 when conservative assumptions are used. The maximum dose-rate from TB-20 appears conservative in the photon-dominated shower regions of stops; however, this is not the case for thick stops, where dose comes primarily from photoneutrons. The Abel Inversion (AI) method provides an accurate estimate of dose radial distribution provided that statistics in the average Cartesian dose profiles are good and the profiles are well behaved. The AI analysis begins to systematically underestimate the dose at deeper target thickness, because the fitting process tends to be less accurate. Rather than fitting a radial distribution to noisy data, it may be best to simply numerically integrate the data.

Regarding contact dose-rate in TB-20, it was found that MARS did not reproduce the results obtained in TB-20 when turning off PNs; however, as shown in Fig. 14, including PNs in the MARS simulations brought the results much closer to the TB-20 modeling. This is most likely because a conservative estimate was used as the initial dose-rate for EGS4; however, the agreement only occurs up to the thickness where PNs do not dominate the dose-rate. Above this thickness, the EGS4 results are no longer conservative.

As for comparisons with PN dose-rate equivalent measurements, MARS simulation results presented in Table 6 are approximately 4-5 times the measured values in beamline 6-ID and close to that measured in 11-ID, see Table 7. We found that at the time the PN measurements were made, beam misalignment in 6-ID would have caused a reduction by a factor of 3 in effective straight section path length and thus also in GB power. Given the additional variability due to fluctuations in Z_{eff} and pressure, the MARS results are in reasonable agreement with measurements. In order to properly model the PN dose (a tertiary product), the simulation requires an accurate measure of undulator beamline Z_{eff} and pressure, as well as the inclusion of collimation by exit masks. Modeling beamline conditions such as pressure with a separate Monte Carlo analysis [25] may be useful for predictive purposes, especially as higher beam currents with the APS upgrade are anticipated.

Using MARS to evaluate the necessary beam stop transverse size within the FOE as previously described in TB-7, indicated that smaller stops do lead to increased dose, however this is mainly in the vicinity of the stop. Thicker targets appear to stop more of the direct GB radiation scattered from the upstream end of the FOE. The best stops in terms of radiation protection would appear to be those of 24-cm-width W. The FE exit masks are found have a significant effect on the dose distribution in the FOE. It may be necessary to complete further studies to verify that shielding is satisfactory before the expected upgrade to 200 mA takes place.

An alternative approach to determine the extremal ray thickness was used with MARS. By varying the radius of a cylindrical Pb target and calculating the dose-rate in the back wall phantom, one could observe the thickness where the direct and Moliere scattered GB radiation was effectively turned off. The beam edge radius of 0.71 cm and a dose break point radius of 2.7 cm indicates that 2.2 cm of Pb as an extremal ray thickness should be sufficient. The simulations indicate an additional thickness of $2R_m$ should be sufficient to shield the extremal ray determined in ray-tracing analysis.

6.2 Computational Considerations

MARS simulations were run for this study using inclusive or weighted events rather than using exclusive or unweighted events. In the former case, if a reaction produces four secondary particles of equal probability, one trajectory is followed with a weighting of 4 rather than for the latter case where all four secondary trajectories are tracked. This weighting process is referred to as importance sampling. Importance sampling reduces the burden on CPU time, but for thick-target simulations where the numbers of tracks become diminished, it can unduly weight individual events and reduce spatial dose accuracy. MARS is well regarded in the high-energy physics community [48]; future upgrades to the program include the implementation of EGS5 for simulating electromagnetic showers [49].

Regarding computing capability, the low levels of radiation simulated here begin to test machine capability and computational accuracy for single runs, even with 10^9 primary events. This limitation can be exceeded with batch submission of multiple MARS jobs. The maximum number of primary events that can be simulated currently with MARS is 2×10^9 . Multiple parallel submissions of MARS jobs can now allow the number of primary events to go higher. In the present work, the average of 10 jobs with each initiated with random seeds provides improved statistics. Due to the fact that the code uses inclusive modeling, large numbers of primary events are necessary to bring the statistical noise down. The speed of data analysis is also a critical parameter when dealing with the large amounts output data that can be generated by simulations. The use of SDDS tools has begun to improve the throughput of data analysis and will continue to reduce the turn-around time between model conception and analyzed results.

References

1. N. Ipe, et al., "Guide to Radiation Beamline Shielding Design at the APS," ANL/APS/TB-7 (1993).
2. P. K. Job, et al., "Bremsstrahlung Scattering Calculations for the Beam Stops and Collimators in the APS Insertion-Device Beamlines," ANL/APS/TB-20 (1994).
3. W. Yun, et al., "Radiation Shielding of Insertion Device Beamlines Using a Mirror as the First Optical Element," ANL/APS/TB-21, February 1995.
4. P. K. Job, et al. "Guidelines for Beamline and Front-End Radiation Shielding Design at the Advanced Photon Source," ANL/APS/TB-44, Rev. 3, September 2008.
5. M. Pisharody, et al., "Dose Measurements of Bremsstrahlung-Produced Neutrons at the Advance Photon Source," ANL/APS/LS-269 (1998).
6. M. Pisharody, et al., Nucl. Instrum. Meth. A, **430**, 542 (1999).
7. N. V. Mokhov and S. I. Striganov, "MARS15 overview," Technical Report Fermilab-Conf-07/008-AD, 2007.
8. N. V. Mokhov et al., "Physics models in the MARS15 code for accelerator and space applications," in *Int. Conf. on Nuclear Data for Science and Technology, AIP Conf. Proc.* **769**, pp. 1618-1623, 2004.
9. M. Pisharody, et al., "Measurement of Gas Bremsstrahlung from the Insertion Device Beamlines of the Advanced Photon Source," ANL Report, ANL/APS/LS-260, ANL, March 1997.
10. W. R. Nelson, "Properties of the EM Cascade," SLAC-PUB-4203, February 1987.
11. ICRU Report 28, *Basic Aspects of High Energy Particle Interactions and Radiation Dosimetry, International Commission on Radiation Units and Measurements*, Washington, D.C., December 1978.
12. H. W. Koch and J. W. Motz, Rev. Mod. Phys., **31**(4), 920 (1959).
13. J. C. Liu, W. R. Nelson, and K. R. Kase, Health Physics **68**(2), 205 (1995).
14. A. Rindi, Health Physics, **42**, 187 (1982).
15. G. Tromba and A. Rindi, Nucl. Instrum. Meth. A, **292**, 700 (1990).
16. Y.-S. Tsai, Rev. Mod. Phys., **46**(4), 815 (1974)
17. W.-M. Yao, et al., Journal of Physics G **33**, 1 (2006).
18. [C. Amsler et al.](http://pdg.lbl.gov/2009/AtomicNuclearProperties/HTML_PAGES/104.html) (Particle Data Group), Physics Letters **B667**, 1 (2008). Available on-line: http://pdg.lbl.gov/2009/AtomicNuclearProperties/HTML_PAGES/104.html

19. N. V. Mokhov, private communication.
20. S. Ban, H. Hirayama, S. Miura, *Health Physics*, **57**, 407 (1989).
21. M. Pisharody, et al., *Nucl. Instrum. Meth. A* **401**, 442 (1997).
22. J. C. Franck, "Bremsstrahlung du Faisceau Stocke sur les molecules Residuelles de la Chambre Avide de Suder ACO," LURE EP 88-01 (1988)..
23. P. K. Job, M. Pisharody, E. Semones, *Nucl. Instrum. Meth. A* **438**, 540 (1999).
24. Y. Asano, et al., *Nucl. Instrum. Meth. A* **451** 685 (2000).
25. P. Berkvens, R. Kersevan and P. Colomp, "Shielding assessment of the optics hutches of the ESRF beamlines," Proc. of the RadSynch07 Workshop, Saskatoon, 2007.
26. B. Rossi, *High-Energy Particles*, Prentice-Hall, Englewood Cliffs, NJ, 1961, p. 223.
27. D. W. O. Rogers, *Health Physics*, **46**(2), 891(1984).
28. ICRP Pub. 51, "*Data for Use in Protection Against External Radiation*," Annals of the ICRP, **17**(2/3), Pergamon, New York, 26 (1987).
29. J. Schwinger, *Phys. Rev.*, **75**(12), 1912 (1949).
30. Y. Asano and N. Sasamoto, *Rad. Protection Dosimetry* **82**(3), pp. 167-174 (1999).
31. J. K. Shultis and R. E. Faw, *Radiation Shielding*, Prentice Hall, Upper Saddle River, NJ, 1996, p. 121.
32. A. Ferrari, M. Pelliccioni, and P. R. Sala, *Nucl. Instrum. Meth. B* **83**, 518 (1993).
33. V. Sajaev, private communication, April 2004.
34. M. Reiser, *The Theory and Design of Charged Particle Beams*, Wiley, New York, 1994, p. 344.
35. M. Pisharody, et al., *Radiation Physics and Chemistry* **59**(2000) 459-466.
36. Y. Asano, "Simulation of Angular Distribution of Gas Bremsstrahlung Depending on the Residual Gas Pressure of Storage Ring," Proc. of the 2nd International Workshop on EGS, 8-12 August 2000, Tsukuba, Japan
37. J. C. Liu, et al., "Calculations of the Giant-Dipole-Resonance Photoneutrons Using a Coupled EGS4-MORSE Code," SLAC-Pub-95-6764, October 1995.
38. I. H. Hutchinson, *Principles of plasma diagnostics*, Cambridge, New York, 1987, p. 124.
39. J. Dutriex, A. Dutriex, and M Tubiana, *Phys. Med. Biol.* **10**(2) (1965) 177-190.
40. J. E. Martin, *Physics for Radiation Protection, A Handbook*, Wiley-VCH, Weinheim, 2006, p. 353.
41. J.H. Hubbell, NSRDS-NBS 29, August 1969.
42. J.H. Hubbell, and S.M. Seltzer, (2004), /Tables of X-Ray Mass Attenuation Coefficients and Mass Energy-Absorption Coefficients/ (version 1.4). [Online] Available: <http://physics.nist.gov/xaamdi> [2008, November 4]. National Institute of Standards and Technology, Gaithersburg, MD.
43. J. T. Collins, et al., "Canted-Undulator Front-End Exit-Mask Flow-Induced Vibration Measurements," Light Source Note ANL/APS/LS-306, Argonne National Laboratory, August 2004.
44. United States Code of Federal Regulation, 10CFR835, April 29, 2009.
45. M. Borland and R. Soliday, "Application Programmer's Guide for SDDS Version 1.5", APS LS Note, June 2006.
46. R. Soliday, private communication, January 2009.

47. J. J. More, B. S. Garbow, K. H. Hillstrom, "User Guide for MINPACK-1," ANL-80-74, Argonne National Laboratory, August 1980.
48. M. Apollonio, et al. (HARP Collaboration), "Forward production of charged pions with incident protons on nuclear targets at the CERN PS," CERN-PH-EP/2009-024, September 15, 2009, (submitted to Physical Review C).
49. N. Mokhov, private communication, September 2009.

Appendix A: Benchmarking MARS

A-1. Comparisons of Gas Bremsstrahlung Photon Density with Target Density

The angular distribution of gas bremsstrahlung photons calculated by MARS was compared with those given by Asano using EGS4 [36]. MARS results present in Figure A-1 are in general agreement with the EGS4 simulations shown in Figure A-2, though noisier.

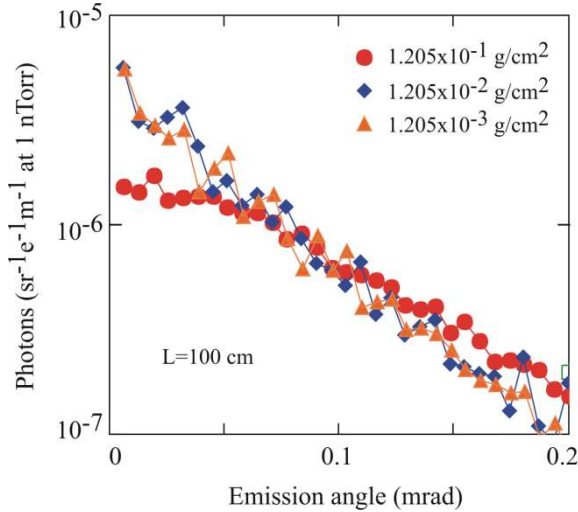


Figure A-1: Photons per electron per steradian per meter of target length from MARS.

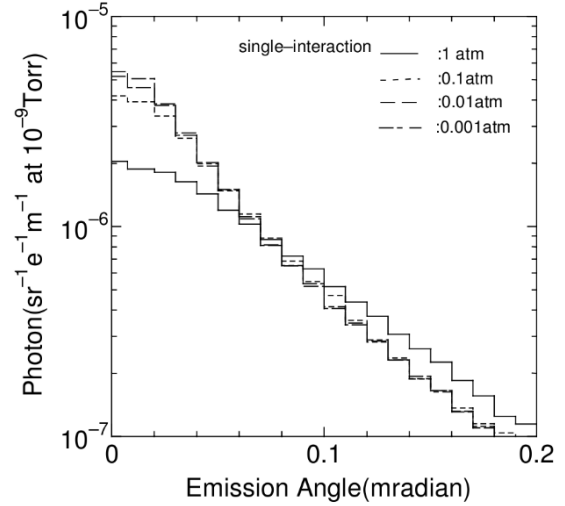


Figure A-2: Photons per electron per steradian per meter of target length from EGS4 (reprinted with permission from Reference 36).

The EGS4 results are specified as having only one interaction in the GB target gas. It was not possible to set this parameter in MARS.

The CPU time increases for low-density, gas bremsstrahlung production targets; variations in CPU speed must also be considered. The following table summarizes the performance of MARS on weed while in MPI mode (parallel processing). Table A-1 presents the average time it takes to follow a single primary trajectory through the simulation including all subsequent daughters. Variations in node processing speeds are not accounted for. In the table, smaller times indicate better performance.

A-2. GB Photon Density and Threshold Electron Energy

The threshold of the electron interaction energy, EMIEL was varied as indicated in Figure A-3. Below the value of EMIEL, the MARS code stops tracking the electron. Note that the minimum setting for this parameter is 100 keV in MARS; whereas in EGS4, it can be as low as 10 keV. Little change is noted in the EGS4 data above 100 keV as seen in Figure A-4; the minimum setting used in MARS was 200 keV. Note that the total electron energy (kinetic + rest mass) is used in EGS4 and presented in Fig. A-4. An

Table A-1: MARS CPU time per 1 primary event in MPI mode (parallel processing) while varying gas bremsstrahlung production target density and length.

$\rho L(\text{g cm}^{-2})$ L (cm)	CPU time per one primary event (μs)			
	1.205×10^{-1}	1.205×10^{-2}	1.205×10^{-3}	1.205×10^{-4}
10 N_{CPU} NEVT	130.1 ± 5.1 15 2×10^8	100.8 ± 2.1 15 2×10^8	100.4 ± 1.5 15 2×10^8	93.15 ± 4.57 15 2×10^9
100 N_{CPU} NEVT	837.9 ± 42.2 5 1×10^8	836.1 ± 41.7 5 1×10^8	975.7 ± 49.0 8 1×10^9	811.1 ± 22.4 8 2×10^9
1000 N_{CPU} NEVT	$7192. \pm 253.$ 15 2×10^8	$6147. \pm 184.$ 15 2×10^8	$7061. \pm 484.$ 12 2×10^8	$7221. \pm 336.$ 12 2×10^8

enhancement at the low-energy end of the spectrum is observed in MARS; though not observed in EGS4, a similar enhancement is observed in FLUKA-generated spectrum to be discussed in the following section.

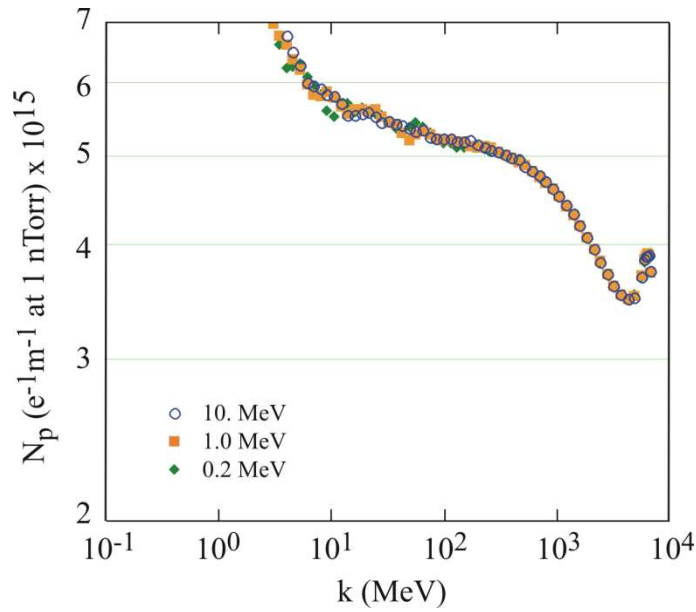


Figure A-3: Normalized GB photon spectra from MARS while varying the electron threshold energy EMIEL. Note the enhancement in photon number below 10 MeV.

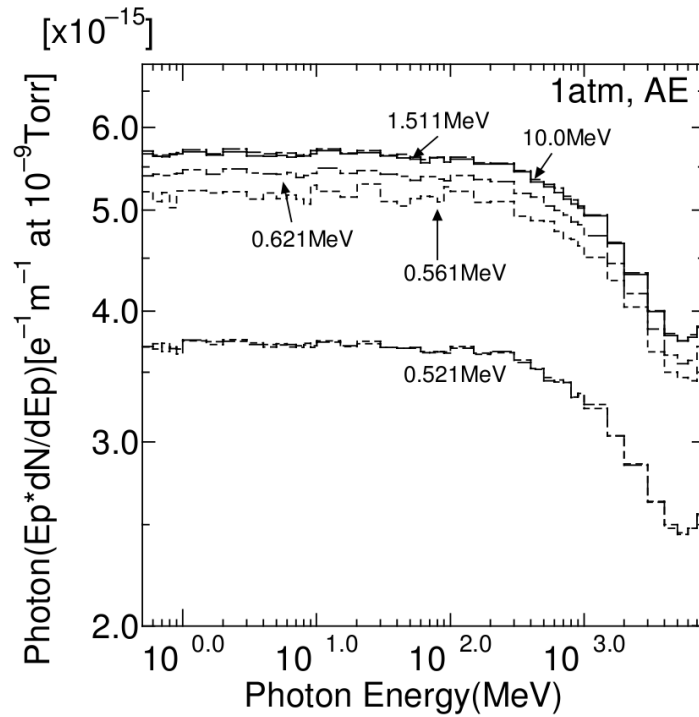


Figure A-4: GB photon spectra with EGS4 varying AE, the minimum cutoff energy for electrons (reprinted with permission from Reference 36). For comparison with Fig. A-3, note that AE includes the electron rest mass energy, whereas EMIEL in Fig A-3 does not.

A-3 PN Production

The production of photoneutron (PNs) is an important function of the MARS code as it relates strongly with radiation protection; therefore we wish to know that it is producing accurate results. We already saw in Section 4 that it produced results within the relatively large errors allowed in the PN measurements. The results of Sheu and coworkers [A1] using FLUKA to model GB in the beamlines of the National Synchrotron Radiation Research Center (NSRRC) in Taiwan are used to compare with MARS. At the NSRRC 1.5 GeV electrons interact with a background gas that is largely diatomic hydrogen. This gas composition, given in Reference A1, was modeled with MARS. The MARS user subroutine LEAK was employed to track neutrons leaving a small (3.85 cm diameter) Pb target 5 cm in length. The comparison is presented in Figure A-5. The peaks of the distributions are in agreement near 1 MeV however, the amplitudes differ by just over an order of magnitude. Based on conversations with the NSRRC author, there may be a factor of 4π unaccounted for in one of the data sets. Using a prescription provided by the MARS author, the number of photons per solid angle is determined as,

$$N_{n_j} = \left(\frac{W_j}{k_s \Omega N_{EVT}} \right) \frac{E_j}{\Delta E_j}, \quad (\text{A-1})$$

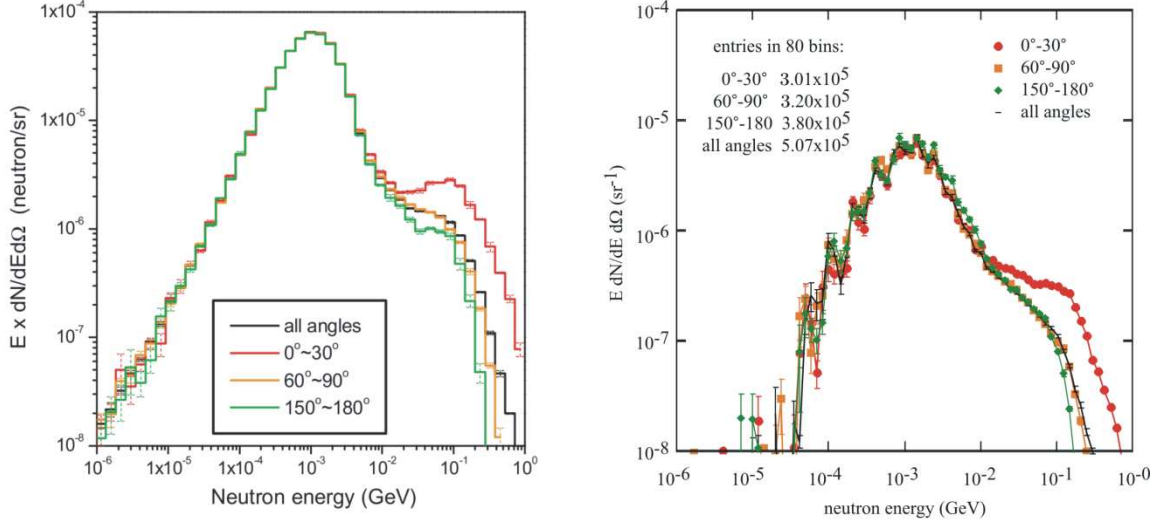


Figure A-5: Comparison of PN production in a Pb target modeled with FLUKA (left) using NSRRC-related parameters and the same geometry with MARS (right). (NSRRC FLUKA results are used with permission from the author.)

where W_j is the summed weight in spectral bin j , E_j is the energy of the j^{th} bin, k_s is the scale factor, Ω the solid angle, N_{EVT} the number of initial trajectories, and ΔE_j the j^{th} bin width. The weight variable averaged over N_f separate runs is expressed as,

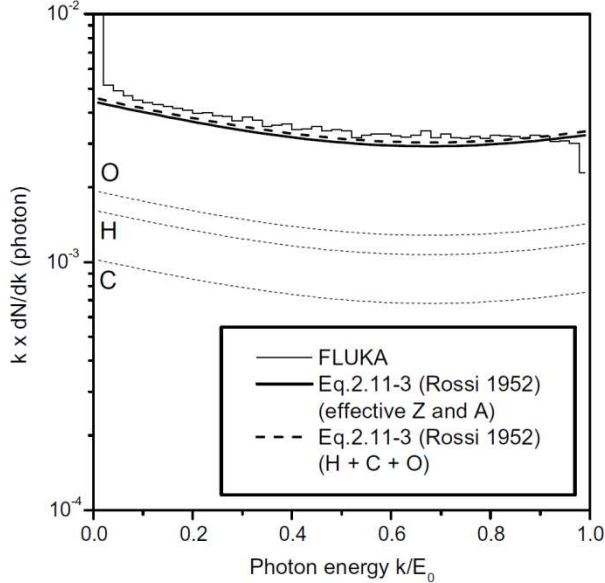


Figure A-6: The GB spectra used to model the NSRRC beamline. Note the enhancement in the low-energy FLUKA spectrum. Ten bins exist between $k/E_0=0$ and 0.2; with an electron energy, $E_0=1.5$ GeV, each bin represents a fixed width of 30 MeV. The first bin shows the enhancement, which is consistent with the MARS results in the previous section. (Data used with permission from the author.)

$$W_j = \frac{1}{N_f} \sum_{k=1}^{N_a} W_{f_{k,2}} \delta(W_{f_{k,1}} = E_j), \quad (\text{A-2})$$

where W_f is an $N_a \times 2$ matrix containing are all the weighted neutron events detected within the solid angle from all runs (column 2) and the energy at which these events occur (column 1). The solid angle is calculated as,

$$\begin{aligned} \Omega &= \Delta\Omega(\theta_2, \theta_1) \\ &= -2\pi(\cos \theta_2 - \cos \theta_1). \end{aligned} \quad (\text{A-3})$$

The data are noisy at the low-energy end of the spectrum. The MARS author suggests using MCNP or MCNPX libraries for neutron transport below 14 MeV; however for the simple geometry of the simulation, these libraries should not be necessary. Nevertheless, based on the results in Section 4, when we have confidence in the experimental conditions, MARS appears to do a reasonably job of predicting neutron dose equivalent.

A-4 Proton Beam Comparisons

The validity of MARS was tested by comparing its output with the results of other analyses. The ability of MARS to model relatively low-energy beam deposition was checked by modeling a proton beam striking a water target phantom. This problem has been examined in the context of evaluating the effectiveness of proton beam radiation therapy [A2]. The authors of this study used the GEANT3 Monte Carlo program for their simulations. MARS output was compared with the published data at 120, 150, 180, and 250 MeV. The longitudinal step sizes were 0.4 cm for the GEANT3 study and 1.0 cm for MARS. A graphical comparison of the Bragg peak locations is presented shown in Figure A-7; and is tabulated in Table A-2. Differences in the location are due to the difference in longitudinal step size: 0.4 cm for GEANT3 and 1.0 cm for MARS.

Table A-2: Comparison of Bragg Peak locations in a water target determined from GEANT3 and MARS.

proton energy (MeV)	Bragg peak location GEANT3 (cm)	Bragg peak location MARS15 (cm)	difference (%)
120	10.2	10.5	2.9
150	15.4	15.5	0.6
180	21.0	21.5	2.4
250	37.0	37.5	1.3

An absolute dose comparison of the proton beam in a water target was made with a simple numerical calculation implemented in MathCAD. The formalism employs linear energy transfer (LET) using restricted mass stopping power (RMSP) data given in Turner [A-3]. The LET data for a 10-keV transfer increment are given in Table A-3 and fit with a fourth-order polynomial over the given range of energies, 0.05-100 MeV, as shown in

Table A-3: Restricted mass stopping power for protons in water at $\Delta E=10$ keV.

E (MeV)	0.05	0.10	0.5	1.0	10.0	100.0
$-\left(\frac{1}{\rho} \frac{dE}{dx}\right)_{10\text{keV}}$ (MeVcm ² /g)	910.	910.	428.	270.	42.2	5.97

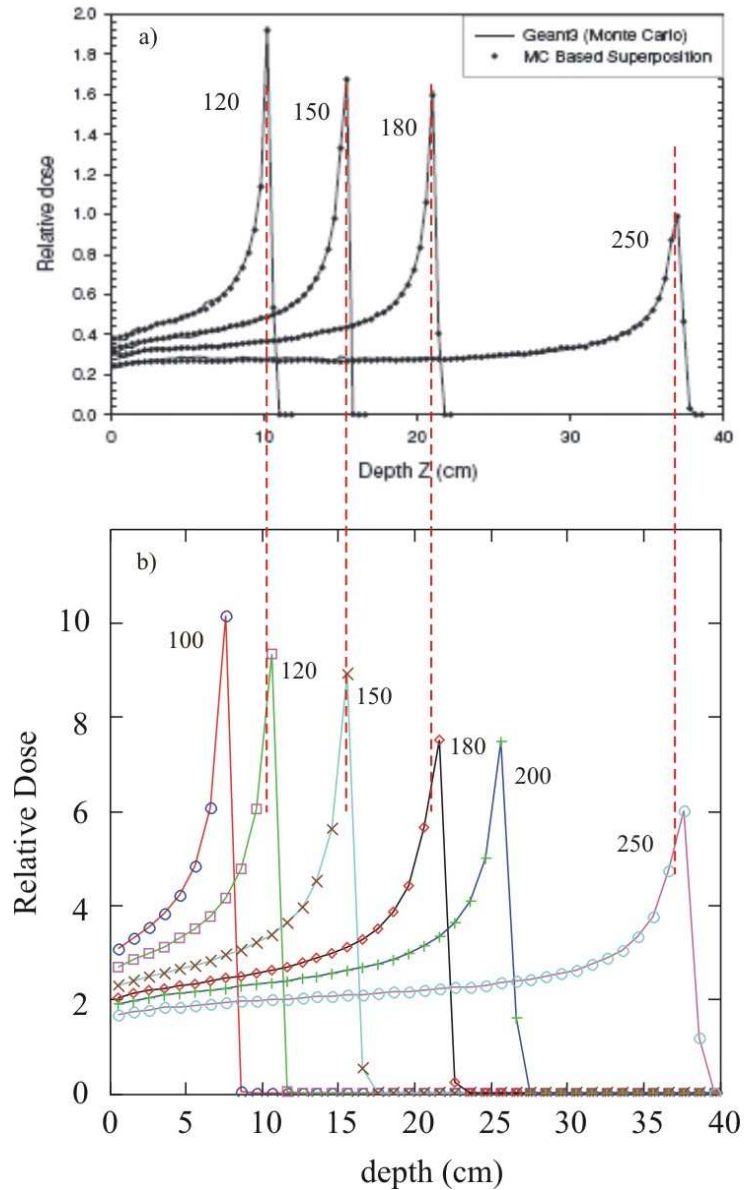


Figure A-7: Comparison of Bragg peak locations determined from a) GEANT3 and b) MARS15 for proton beam energies indicated in MeV in a water target. Longitudinal step size is 0.4 cm in the GEANT3 simulation and 1.0 cm in MARS. The GEANT3 data are reprinted with permission from Reference A2, Fig. 1(a); copyright 2005, IOP Publishing, Bristol, UK.

Figure A-8. Using the LET function generated by the fit, the algorithm calculates the width of each longitudinal step for the fixed energy increment. The beam energy is then decremented by this energy step, and the process repeated until the beam energy is zero. The number of increments per unit distance traveled in the water target then determines the dose. A comparison of dose calculated from the energy deposition algorithm with a MARS15 simulation for a 100 MeV proton beam is presented in Figure A-9. The initial proton beam current is 1 μA . The location of the Bragg peak differs for the two cases, as expected. In the Turner model, energy increments are simply subtracted from a monoenergetic beam; whereas, MARS takes into account the spatial broadening and increasing energy spread of the beam due to interactions with the water. At higher energies, the two methods predict almost identical energy deposition in the water target. Beam spreading is indicated by the dose-rate histograms presented in Figure A-10, again for 1 μA . In this case, for initial proton energies of 120 and 180 MeV, the growth in the transverse extent of the dose is evident as the beam travels from left to right through the water target. Note that dose is tracked in only the central 20 cm of the water target about beam elevation.

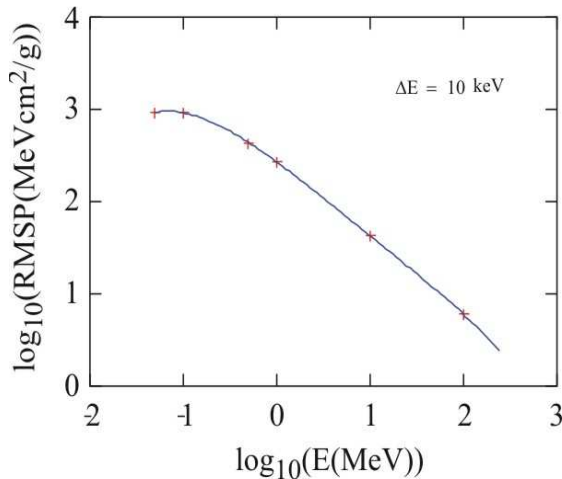


Figure A-8: RMSP data for protons in water with a 4th-order polynomial fit.

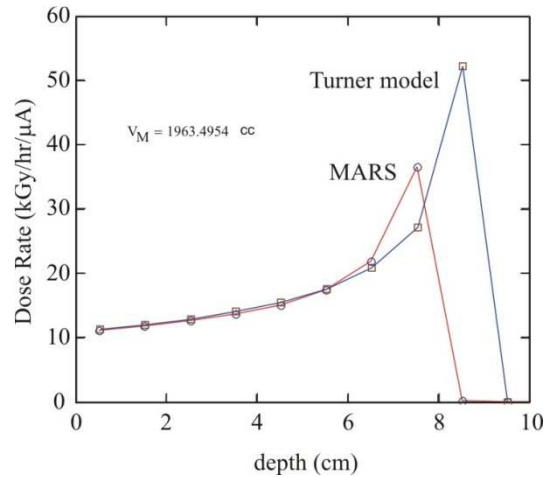


Figure A-9: Comparison of the Turner model and MARS15 simulation of absorbed dose for 100 MeV protons in water.

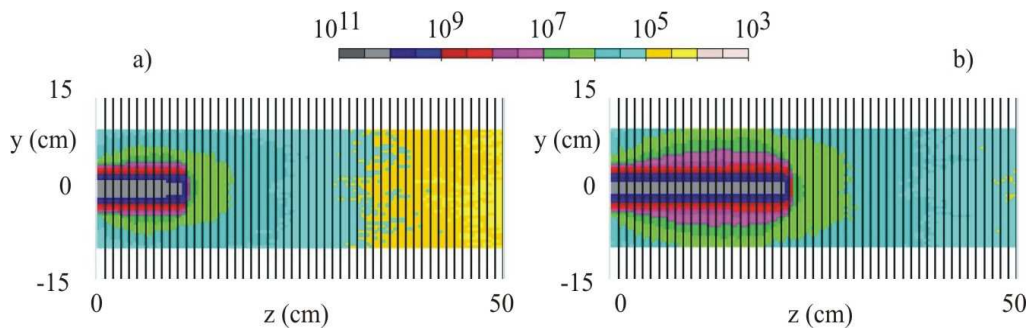


Figure A-10: a) 120 MeV and b) 180 MeV proton beam dose-rate in water calculated by MARS (mSv/hr). The proton beam current is 1 μA in both cases.

The purpose of these two studies is to test the basic validity of MARS in terms of energy deposition and conservation. In the latter of the two comparisons, energy deposition in water is directly compared with a simple numerical algorithm. In both cases, MARS results are in good agreement the alternate approach, within the accuracy of the model.

References

- A1 R.J. Sheu, J.P. Wang, R.D. Sheu, S.H. Jiang, Nucl. Instrum. Meth. B **217**, 555–563 (2004).
- A2. J. S. Li, B. Shahine, E. Fourkal, C. M. Ma, “A particle track-repeating algorithm for proton beam dose calculation,” Phys. Med. Biol., **50**(5), 1001 (2005).
- A3. J. E. Turner, *Atoms, Radiation, and Radiation Protection*, (McGraw-Hill, New York: 1992) p. 105.

Appendix B: TB-20 Extremal Ray Methodology—Results with MARS

The simulation technique used at the APS to determine the Pb thickness required to shield against the extremal ray was initially that presented in TB-20 using EGS4. In TB-20, a solid copper scatterer is placed directly in the path of the GB radiation. The copper fills the full aperture and wall thickness of the 5 cm O.D. beam pipe. Dose is recorded in a phantom in contact with the edge of the beam pipe (Cu). Lead shielding is then placed around the copper and dose is again recorded, this time with the phantom translated 30 cm from the edge of the beam pipe. The simulation then determines phantom dose as a function of shielding thickness.

In TB-20, a contact, no Pb dose-rate of 30 $\mu\text{Sv/hr}$ was obtained in the EGS4 simulation; however, this did not account for the dose due to neutrons. In TB-20, a limiting dose of 500 mrem/year (5 mSv/year) was used. The limiting dose was assumed to be spread uniformly over 2000 hours for an equivalent hourly rate of 0.25 mrem/hr (2.5 $\mu\text{Sv/hr}$). The absence of neutrons in the EGS4 simulation was accounted for by assuming that they represented one-half of the total dose, and therefore the limit for photons modeled by EGS4 was set at 0.125 mrem/hour. MARS on the other hand, includes neutrons in the total dose; thus, to compare the MARS results with those from EGS, the limiting dose here was kept at 0.25 mrem/hr and the contact dose from EGS4 was multiplied by 2 or 60 $\mu\text{Sv/hr}$. The TB-20 geometry is presented in Figure B-1.

In TB-20, it was reported that the dose falls below the limiting value of 2.5 $\mu\text{Sv/hr}$ for a Pb shielding thickness of 4.4 cm; therefore 4.5 cm was recommended as the extremal ray requirement.

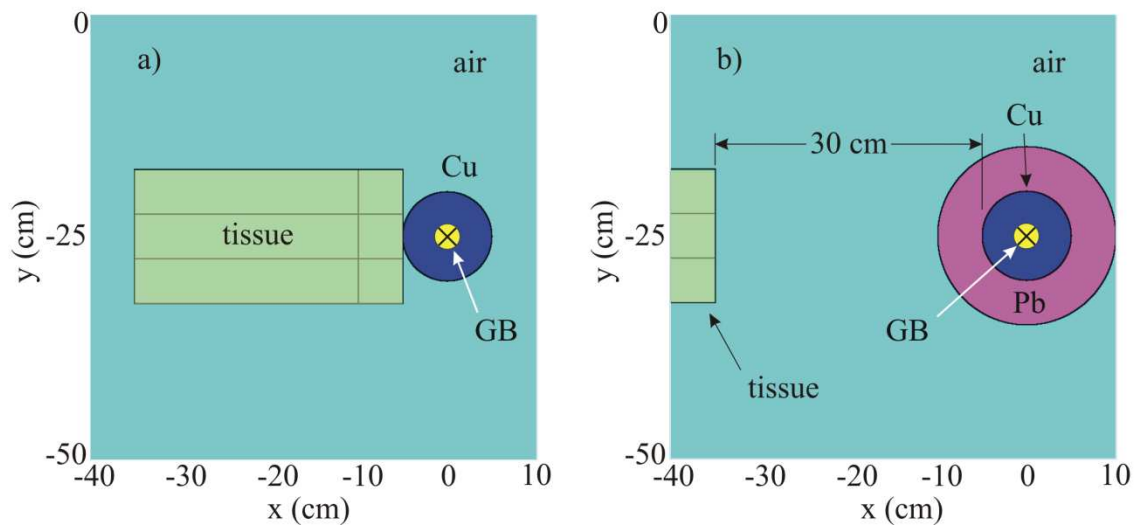


Figure B-1: TB-20 extremal ray geometry used with EGS4 and initially MARS. a) Contact dose with “beam pipe” filled with copper scatterer, and b) phantom moved 30 cm from beam pipe edge with Pb shielding. The direction of the GB beam is into the page.

DRAFT

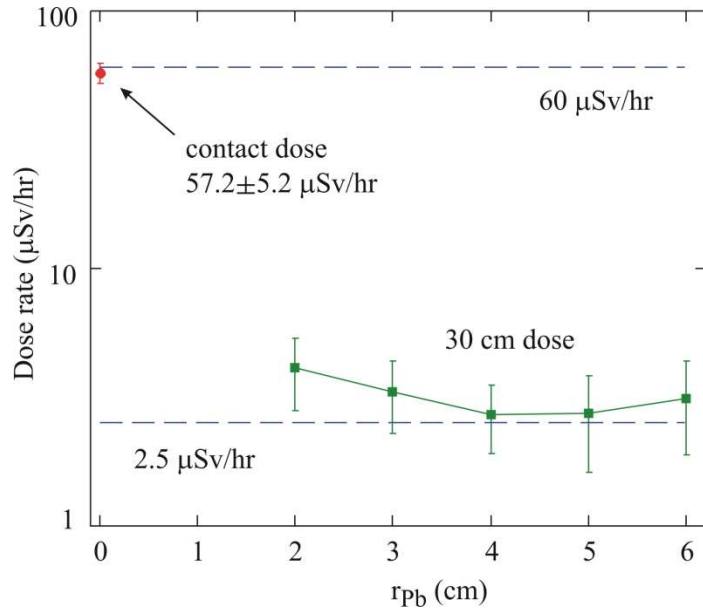


Figure B-2: Extremal ray MARS dose calculations using TB-20 geometry.

Figure B-2 shows simulation results of the TB-20 geometry using MARS; the dose-rate as a function of Pb shielding thickness approaches, but never crosses, the 2.5- $\mu\text{Sv/hr}$ limit, most likely due to the presence of neutrons not included in the EGS4 simulations. MARS calculations in Fig. B-2 indicate that, for Pb shielding in the configuration shown in Fig. B-1, little if any mitigation of the dose-rate in the phantom tissue is achieved by increasing the thickness of the Pb beyond 4 cm. This reduced shielding efficacy is due to the fact that heavy metals such as Pb are poor neutron shielding materials.

Regarding the determination of the minimum distance required between the GB radiation extremal ray and the edge of heavy metal stops and collimators, the geometry used in TB-20 (shown in Fig B-1) was replaced with the more realistic configuration presented in section 5.4, where the stop/collimator is inside the white beam enclosure (FOE), and the dose-rate is calculated outside this shielded enclosure.

Appendix C: Examples of MARS Input Files Used to Model the First Optics Enclosure

Several input files are necessary to run MARS simulations; these include the MARS.INP, GEOM.INP, and the XYZHIS.INP files; examples of these files for the FOE are presented below. The other files (not shown) include m1507.f, the main and user subroutine file, and GNUmakefile which instructs the system on compilation of the executable (e.g., single- or multiprocessor mode).

MARS.INP

The MARS.INP file provides global run parameters (number of events, beam energy, etc) material specification and overall and standard geometry regions. See the MARS manual, Sections 3 and 4 for parameter definitions.

Contact Dose Calculation for TB-44 review. JCD/10/01/01
/share/mokhov/restricted/mars15/dat

INDX 3=T

C CTRL 3=1
C RZVL 5=5.E8
C TAPE 18

CTRL 0
NEVT 2E8

SEED 35415027

C default SEED value: 54217137 (octal--no digits greater than 7)

ENRG 1=7.0
C BIAS 6=0. 7=0. 8=0.
C
C INIT 3 starts at z=-2450 cm for a 10 cm air target (centered), -2464
cm for a 24 cm air target
C (original, not centered), -2514 cm for a 100 cm target (should be -
2490 cm for centered target),
C and -2940 cm for a 1000 cm (10 m) target (centered). Would be -3209
cm for a
C 1538 cm (15.38 m) target (centered), but not doing this; takes too
long to run--jcd 091228.
C
INIT 2=-15.0 3=-2464.
IPIB 10
SMIN 0.01 3.0
C ZMIN=-2490.
ZMIN=-2464.
NLNG 1
ZSEC 820.
C ZSEC -110.
2501=0

DRAFT

C-1

```

NLTR 1
RSEC 225.
C RSEC 40.
C NOBL 1
C RZOB
NMAT 7
MATR 'CU' 'TISS' 'AIR' 'PB' 'CONC' 'VAC' 'W'
C MTDN 3=1.
MTDN 3=0.001205

VARS 4=1.873E18
NHBK 1

```

STOP

GEOM.INP

The GEOM.INP file defines the extended geometry used to define the FOE. The fields and geometry types are provided in the MARS manual, Sections 3 and 4.

Modified FOE beam stop, air-bremmstrahlung source, TB-7 (TB-44) JCD
09/11/29

```

!OPT
!VNAME  TYP XM IM  X0      Y0      Z0      C1      C2      C3
NX  NY  NZ
!
! Safety Shutters
!
bxWssAp  1  0  0   0.    -15.    -180.    3.60    1.00    65.0
bxWssUS  1  0  7   0.    -15.    -180.   10.00    3.75    30.0
bxWssDS  1  0  7   0.    -15.    -145.   10.00    3.75    30.0
!
! Slit mask main body drawing 4105091505-830001, Rev. 03
!
bxCuMskT 1  1  1   0.    -12.476  72.93   3.846    1.322    27.97
bxCuMskB 1  2  1   0.    -17.524  72.93   3.846    1.322    27.97
bxCuMskL 1  3  1   2.947 -15.00   72.93   0.902    3.846    27.97
bxCuMskR 1  4  1  -2.947 -15.00   72.93   0.902    3.846    27.97
bxApMnMk 1  0  0   0.    -15.00  100.75   0.225    0.225     0.25
bxCuMnMk 1  0  1   0.    -15.00  100.75   3.848    3.846     0.25
cyApMkBC 2  0  0   0.    -15.00  104.146  0.0      2.063    0.551
bxCuMkTd 1  2  1   0.    -14.275  100.90   0.5      0.5      3.747
bxCuMkBd 1  1  1   0.    -15.725  100.90   0.5      0.5      3.747
bxCuMkLd 1  5  1   0.725 -15.00   100.90   0.5      0.5      3.747
bxCuMkRd 1  6  1  -0.725 -15.00   100.90   0.5      0.5      3.747
bxCuApet 1  0  0   0.    -15.00   72.93   2.045    1.202    27.97
bxCuAped 1  0  0   0.    -15.00  100.90   0.50     0.50     3.747
bxCuFilU 1  0  1   0.    -15.00   72.93   3.848    3.846    31.717
!
! M4-30 APS 2 mm x 3 mm Water-cooled fixed mask assembly drawing
! 4105091004-300000, Rev. 02 and Pb collimator in FOE.
!
elliApet 6  0  0   0.    -15.00  106.0    0.15     0.10     0.
15.76

```

DRAFT

```

coneApet 4 0 0 0. -15.00 106.0 0. 0.518 0.
0.1 14.05
bxCuMask 1 0 1 0. -15.00 106.0 3.175 3.175 15.76
bXPbapet 1 0 0 0. -15.00 221.76 0.75 0.75 30.00
bXPbColl 1 0 6 0. -15.00 221.76 15.0 10.00 30.00
!
! Vacuum pipe, target/beam stop, and contact phantom
!
ape-4v 1 0 0 0. -15. -80. 3.90 1.30 755.
!cyl-Pb 2 0 4 0. -15. 675. 0.00 3.00 30.
box-PbW 1 0 7 0. -15. 675.0 10. 10.0 30.
box-2t 1 0 2 0. -15. 705.0 10. 10.0 5. 5
5 1
box-3t 1 0 2 0. -15. 710.0 10. 10.0 25. 1
1 1
!
! Tissue phantom volumes along outer walls
!
box-Tts 1 0 2 0. 201.2 -80.0 15.0 15.00 860.0
box-Sts 1 0 2 -136.9 -15.0 -80.0 15.0 15.00 860.0
boxBHts 1 0 2 0. -15. 780.0 151.9 15.00 30.0
boxBVts 1 0 2 0. 10.6 780.0 15.0 175.60 30.0
!
! FOE volume
!
box-vac 1 0 6 -30.00 15.00 0. 90.00 170.0 770.
!
! Ratchet wall
!
box-5Pb 1 0 4 0. -15.635 -80. 20.32 20.955 12.065
box-6Pb 1 0 4 0. -15.635 -67.935 20.32 20.955 12.065
box-7Pb 1 0 4 0.00 -15. -55. 17.145 17.621 5.08
box-8Pb 1 0 4 0. -15. -50. 7.874 6.35 40.0
box-vac 1 0 6 0. -15. -80.0 17.78 17.78 80.
!
! FOE walls floor and ceiling
!
bXPbwlb 1 0 4 -30. 15. 770.0 90.0 170.0 5.
bXPbwla 1 0 4 0. -15. 775.0 50.0 50.0 5.
bXPbwll 1 0 4 -120.95 15. 0.0 0.95 170.0 775.
bXPbwlr 1 0 4 -30.95 185.6 0.0 90.95 0.6 775.
box-con 1 0 5 -2.95 0.6 -80. 118.95 185.60 855.
!
! Air source and wrapper volumes
!
cyl-air 2 0 3 0. -15. -2464. 0.0 5.0 24.0
cyl-vac 2 0 0 0. -15. -2440. 0.0 5.0 2360.0
cyl-vac 2 0 0 0. 0. -180. 0.0 225.0 1000.0

TR1 0. 0. 0. 2. 0. 0.
TR2 0. 0. 0. -2. 0. 0.
TR3 0. 0. 0. 0. -3.735 0.
TR4 0. 0. 0. 0. 3.735 0.
TR5 0. 0. 0. 0. 2.0 0.
TR6 0. 0. 0. 0. -2.0 0.

```

stop

```
cyl-4a  2  2  4  0. -40. 125.  0.  5.  25.  5  2  ! cyl-4a
VNAME  TYPE TRF IM  X0  Y0  Z0  C1  C2  C3  NZ  NR
```

XYZHIS.INP

The XYZHIS.INP file defines histogram “detectors” that are used to collect different types of radiation in various presentations; for example, histograms may be used to sample dose, collect particle spectra, or record particle fluence. These detectors are essentially independent of the GEOM.INP definitions; however, dose equivalent histograms (DEG, DEN, DET, etc.) must be specified in geometry regions occupied by tissue phantoms. Consult the MARS manual, Section 10 for ranges and definitions.

```
XYZ histo TB7 (TB44) 2008-Sept-01, modified 2009-Dec-23 JCD

xyz  -12.0  12.0  -27.0  -3.0  675.  705.  120 120  1
XY_Pb_shower
DEE DEN DEG DET

xyz  -12.0  12.0  -27.0  -3.0  675.  735.  1 120 120
YZ_Pb_shower
DEE DEN DEG DET

xyz  -150.  150.  -27.0  -3.0  -180.  820.  150  1 200
XZ_air_shower
FLE FLM FLN FLG DEN DEG DET

xyz  -12.  12.  -170.  220.  -180.  820.  1 195 200
YZ_air_shower
FLE FLM FLN FLG DEN DEG DET

xyz  -5.  5.  -20.  -10.  -2464. -2400.  51  1 120
XZ_air_shower
FLE FLG

xyz  -10.5  10.5  -25.5  -4.5  705.  706.  21  21  1 XYZ in
tiss
FLE FLN FLG FLM DEE DEG DEN DET
!
xyz  -5.  5.  -20.  -10.  -2425. -2420.  1  1  1 e,g, & n
spectra in GB
SPE SPG SPN
```

stop

```
! XYZ X1 X2 Y1 Y2 Z1 Z2 NX NY NZ TEXT
! Histo types (1-32):
C STA- star density          E>50 MeV (cm^-3 s^-1)
C DRE- 30d/1d residual dose on contact (mSv/hr)
C FLT- total flux of hadrons  E>ETFH (cm^-2 s^-1)
C FLP- flux of protons       E>ETFH (cm^-2 s^-1)
C FLN- flux of neutrons      E>ETFN (cm^-2 s^-1)
C FLK- flux of pions/kaons   E>ETFH (cm^-2 s^-1)
C FLM- flux of muons         E>ETFM (cm^-2 s^-1)
C FLG- flux of photons       E>ETFG (cm^-2 s^-1)
```

DRAFT

```

C FLE- flux of e-e+           E>ETFE   (cm^-2 s^-1)
C
C DAB- absorbed dose         (Gy/yr)   at 2.e7 s/yr
C DPA- DPA                    (DPA/yr)  at 2.e7 s/yr
C
C DET- FTD prompt dose equivalent, total (mSv/hr)
C DEP- FTD prompt dose equivalent, proton (mSv/hr)
C DEN- FTD prompt dose equivalent, neutron (mSv/hr)
C DEK- FTD prompt dose equivalent, pi/K (mSv/hr)
C DEM- FTD prompt dose equivalent, muon (mSv/hr)
C DEG- FTD prompt dose equivalent, photon (mSv/hr)
C DEE- FTD prompt dose equivalent, e+e- (mSv/hr)
C
C PDT- power density, total (mW/g or Gy/s)
C PDP- power density, proton (mW/g or Gy/s)
C PDN- power density, neutron (mW/g or Gy/s)
C PDK- power density, pion/kaon (mW/g or Gy/s)
C PDM- power density, muon (mW/g or Gy/s)
C PDG- power density, photon (mW/g or Gy/s)
C PDE- power density, e-e+ (mW/g or Gy/s)
C
C Don't use DLT: it is extremely slow now!!!
C DLT- instantaneous temperature rise (degC or degK) per AINT
(ppp)
C
C Default cutoff energy is used for spectra:
C
C SPP- proton energy spectrum (GeV^-1 cm^-2 s^-1)
C SPN- neutron energy spectrum (GeV^-1 cm^-2 s^-1)
C SPK- pion/kaon energy spectrum (GeV^-1 cm^-2 s^-1)
C SPM- muon energy spectrum (GeV^-1 cm^-2 s^-1)
C SPG- photon energy spectrum (GeV^-1 cm^-2 s^-1)
C SPE- e+e- energy spectrum (GeV^-1 cm^-2 s^-1)
C
! In any run: Sum_detectors (Sum_types) =< nof_histmax (=300, default)

```

DRAFT